Journal Pre-proofs

The Bajgan Complex revealed as a Cretaceous ophiolite-bearing subduction complex: A key to unravel the geodynamics of Makran (southeast Iran)

Luca Pandolfi, Edoardo Barbero, Michele Marroni, Morteza Delavari, Asghar Dolati, Maria Di Rosa, Chiara Frassi, Antonio Langone, Federico Farina, Christopher S. MacDonald, Emilio Saccani

PII: S1367-9120(21)00303-5
DOI: https://doi.org/10.1016/j.jseaes.2021.104965
Reference: JAES 104965

To appear in: *Journal of Asian Earth Sciences*

Received Date: 21 April 2021
Revised Date: 24 September 2021
Accepted Date: 9 October 2021

Please cite this article as: Pandolfi, L., Barbero, E., Marroni, M., Delavari, M., Dolati, A., Di Rosa, M., Frassi, C., Langone, A., Farina, F., MacDonald, C.S., Saccani, E., The Bajgan Complex revealed as a Cretaceous ophiolite-bearing subduction complex: A key to unravel the geodynamics of Makran (southeast Iran), *Journal of Asian Earth Sciences* (2021), doi: https://doi.org/10.1016/j.jseaes.2021.104965

The Bajgan Complex revealed as a Cretaceous ophiolite-bearing subduction complex: a key to unravel the geodynamics of Makran (southeast Iran)

Luca Pandolfi[1,2], Edoardo Barbero [3], Michele Marroni [1,2], Morteza Delavari[4], Asghar Dolati [4], Maria Di Rosa [1], Chiara Frassi [1], Antonio Langone[5], Federico Farina [6], Christopher S. MacDonald [7], Emilio Saccani[3]

1 Dipartimento di Scienze della Terra, Università di Pisa, Via S. Maria 53, 56126 Pisa, Italy

2 Istituto di Geoscienze e Georisorse, CNR, Pisa, Via G. Moruzzi 1, 56124 Pisa, Italy

3 Dipartimento di Fisica e Scienze della Terra, Università di Ferrara, Via Saragat 1, 44123 Ferrara, Italy

4 Faculty of Earth Sciences, Kharazmi University, Shahid Mofatteh St. 43, Tehran, Iran

5 Istituto di Geoscienze e Georisorse, CNR, Sezione di Pavia, Via Ferrata 1, 27100 Pavia, Italy

6 Dipartimento di Scienze della Terra "Ardito Desio", Università di Milano, Via Luigi Mangiagalli, 34, 20133 Milano, Italy

7 School of Earth and Space Exploration, Arizona State University, 781 Terrace Mall, Tempe, AZ 85287, USA

Corresponding author:

Prof. Michele Marroni

Dipartimento di Scienze della Terra,

Università di Pisa, Via S. Maria, 53

56126 Pisa, Italy.

E-Mail:michele.marroni@unipi.it

Abstract

In the Makran area, a wide accretionary wedge is originated by the north-dipping subduction of the Neo-Tethyan oceanic lithosphere. The rear of the accretionary wedge is represented by the North Makran Domain that consists of an imbricate stack of tectonic units derived from the closure of the North Makran oceanic basin. This oceanic basin opened southward of the Eurasia continental margin during the Early Cretaceous. The Bajgan Complex is interpreted as an Early Paleozoic or older metamorphic basement representing the remnants of the Bajgan-Durkan continental microplate located at the southern rim of the North Makran oceanic basin. This microplate plays thus a key-role in the so far proposed reconstructions of the evolution of the whole Makran area.

The Bajgan Complex consists of Late Jurassic to Early Cretaceous meta-ophiolites and related meta-sediments, both affected by HP-LT metamorphism. The HP-LT metamorphism has been overprinted by epidote amphibolite to greenschist facies metamorphism in the Late Cretaceous during the progressive exhumation of the Bajgan Complex up to shallow structural levels. The incompatible trace elements ratios of meta-igneous rocks indicate a subduction-unrelated chemical affinity for these meta-ophiolites.

Our study clearly indicates that the Bajgan Complex cannot be considered as a continental basement of pre-Mesozoic age. Consequently, the closure of the North Makran oceanic basin cannot be related to a collision between a microcontinent and the continental margin of the Lut Block.

Key-words: meta-ophiolites, metamorphism, geochemistry, subduction, Bajgan Complex, Makran, Iran

1. Introduction

Subduction complexes represent fossil accretionary wedges developed at convergent margins where materials of the down-going ocean plate are accumulated by off-scaping and underplating processes adjacent to the leading edge of the upper plate (e.g., von Huene and Scholl, 1991; Kusky et al., 2013; Ruh, 2020). At depth, the subduction complexes are thus characterized by rock assemblages deformed under high pressure-low temperature (HP-LT) metamorphic conditions (e.g., Agard et al., 2009). They may supply useful informations for the geodynamic reconstructions of the area, as for example the location and onset age of the subduction zones, the age of the oceanic lithosphere involved into the convergence, the accretion mechanisms, the timing of the subduction-related metamorphism and the exhumation processes. The identification of the fossil subduction complexes is thus crucial for the reconstruction of the geodynamic history of the worldwide orogenic belts.

In the Makran area, SE Iran (Fig. 1), a wide accretionary wedge orginated by the north-dipping subduction of the Neo-Tethyan oceanic lithosphere beneath the Southern Eurasian continental blocks, i.e. the Central Iran, Lut and Afghan Blocks, is exposed on-land (e.g., McCall and Kidd, 1982; McCall, 1985; 1997; Platt et al., 1985; Burg et al., 2008). The rear of the accretionary wedge is represented by the North Makran Domain that consists of an imbricate stack of weakly deformed and metamorphosed tectonic units, dominated by Early Cretaceous ophiolite units as well as Late Cretaceous tectonic and sedimentary mélanges (McCall, 1985; 2002). The North Makran Domain also includes the Bajgan Complex, that in the literature is interpreted as an Early Paleozoic or older metamorphic continental basement belonging to the Bajgan-Durkan microplate (e.g., McCall and Kidd, 1982; Dorani et al., 2017), even if the data supporting this interpretation are lacking at all. It is important to outline that the occurrence of

continental basement in the North Makran Domain can establish a first-order constraint for all the so far proposed geodynamic reconstructions (Hunziker et al., 2015; Saccani et al., 2018; Burg, 2018; Monsef et al., 2019).

This paper provides a new multidisciplinary dataset on the Bajgan Complex, including lithostratigraphic and structural constraints as well geochemical, geochronological and P-T estimate on the meta-igneous rocks, as well as P-T estimations and geochronology constraints. Our study allows to re-intepret the Bajgan Complex as Late Jurassic to Early Cretaceous meta-ophiolites and related pelagic meta-sediments that were affected by HP-LT metamorphism within a Cretaceous subduction complex. These conclusions strongly contrast with the current interpretations, which consider the Bajgan-Durkan complex the relicts of a continental microplate. Consequently, a novel geodynamic scenario where the Bajgan Complex is interpreted as subduction complex is required. In addition, our study provides also new constraints for the subduction initiation in the Makran area during the Late Cretaceous

2. Geodynamic framework of the Makran region

In the Makran region, SE Iran (Fig. 1), one of the largest worldwide accretionary wedge is exposed for c. 1000 km along strike from west to east (McCall and Kidd, 1982; Bayer et al., 2006; Burg et al., 2013; Haberland et al., 2021). The southern boundary of this accretionary wedge is represented by the north-dipping and low-angle subduction zone of the oceanic lithosphere of the Oman Sea whereas the northwestern one is represented by the continental margin of the Lut Block. In this framework, the rear of the Makran accretionary wedge is represented by the North

Makran Domain (Fig. 2) that consists of a stack of tectonic units, all deformed and metamorphosed during the pre-Eocene tectonics (McCall, 1997; Burg, 2018).

The geodynamic reconstruction of the North Makran Domain has been recently reconsidered in several papers (Dolati and Burg, 2013; Hunziker et al., 2015; Saccani et al., 2018; Barrier et al., 2018; Burg, 2018; Monsef et al., 2019). All these reconstructions indicate that the north-dipping subduction of the Neo-Tethys oceanic lithosphere below the southern margin of the Lut Block was already active before the Early Cretaceous. This subduction led to the formation of an embryonal and likely intra-oceanic volcanic arc located close ~~in~~ the southern rim of the Lut Block during the Early Cretaceous (Saccani et al., 2018). Simultaneously, the slab retreat produced the opening of a supra-subduction oceanic basin (i.e. the North Makran Ocean) leading to the separation of a continental ribbon, i.e. the Bajgan-Durkan complex, from the Lut Block (Hunziker et al., 2015; Saccani et al., 2018). According to Saccani et al. (2018), the convergence in the North Makran Oceanic basin started in the uppermost Late Cretaceous as a consequence of the collision between an oceanic plateau built-up on the Neo-Tethys crust and the north-dipping subduction zone. This event resulted in a subduction jump toward the south, but also in the closure of the North Makran Oceanic basin that occurred before the Early Eocene. Recently, Barbero et al (2020a) have further suggested that the closure of the North Makran Oceanic basin occurred by a new north-dipping subduction located at the northern rim of this ocean.

All the proposed reconstructions are based on the geodynamic interpretation of the six different tectonic units recognized in the North Makran Domain. From south to north and from bottom to top, these units include (Fig. 2): 1) the Coloured Mélange, also known as the Imbricate Zone of Burg et al. (2013) or Coloured Mélange Complex of Saccani et al. (2018); 2) Sorkhband and Rudan ophiolites (also known as southern ophiolites); 3) the Bajgan-Durkan Complex (recently divided in Bajgan Complex and Durkan Complex; Barbero et al., 2021); 4) the Deyader

Complex; 5) the North Makran ophiolites (also known as northern ophiolites) 6) the Ganj Complex. The main deformations in these units are sealed by the Early Eocene sedimentary successions clearly indicating that the North Makran Domain has been extensively deformed during the pre-Eocene tectonic evolution of the Makran (see also McCall, 1985, 2002).

The development of the Coloured Mélange occurred in the late Paleocene, probably during the final stage of the collision of an oceanic plateau with the southern rim of the Bajgan-Durkan continental microplate (Saccani et al., 2018; Burg, 2018).

The North Makran ophiolites are Early Cretaceous in age and represent the remnants of the North Makran Oceanic basin (e.g., McCall and Kidd, 1982; McCall, 2002; Burg, 2018; Delavari et al., 2016; Saccani et al., 2018). They include three tectonic units, which are: 1) the Band-e-Zeyarat ophiolite (Ghazi et al., 2004; Barbero et al., 2020b); 2) the Remeshk-Mokhtarabad ophiolite (Moslempour et al., 2015; Monsef et al., 2019); 3) the Fannuj-Maskutan ophiolite (Desmons and Beccaluva, 1983). The North Makran ophiolites are overthrust by the Late Cretaceous HP-LT Deyader Complex consisting of meta-ophiolites and their meta-sedimentary sequences (McCall, 1985; Hunziker et al., 2015; Omrani et al., 2017). This complex is in turn thrust by the Ganj Complex recently re-interpreted as a Turonian-Coniacian volcanic arc formed in an extensional intra-arc setting located in the southern margin of the Lut Block (Barbero et al., 2020a). This hypothesis agrees with provenance data from Late Cretaceous to Miocene turbidites that point out for the existence of a Late Cretaceous – Eocene volcanic arc in the Makran area (Mohammadi et al., 2016, 2017). The North Makran ophiolites as well as the Ganj Complex and the Bajgan-Durkan Complex are thrust on the Coloured Mélange Complex (Gansser, 1959; McCall, 1983; Saccani et al., 2018).

The Bajgan-Durkan Complex plays an important role for the Makran geology as is thought to represent the relicts of a small continental microplate detached from the Lut Block and located

south of the North Makran oceanic basin (e.g., McCall and Kidd, 1982; McCall, 1985; Hunziker et al., 2015; Burg, 2018). Barbero et al. (2021) have demonstrated that the Durkan Complex consists of several tectonic slices derived from highly deformed Early Cretaceous – Paleocene carbonatic and volcanic successions interpreted as the remnants of oceanic seamounts. The Bajgan Complex (i.e., the topic of this paper) is described as an assemblage of metamorphic rocks derived from sedimentary and magmatic protoliths of Paleozoic age or older (McCall, 1985; Dorani et al., 2017), so far interpreted as the metamorphic basement of a continental microplate (e.g., McCall, 1985; Hunziker et al., 2015). According to these authors, deformation of the Bajgan Complex occurred during the continent-continent collision between the Bajgan-Durkan microplate and the Lut Block during the closure of the North Makran Oceanic basin (McCall, 1983; Omrani et al., 2017; Dorani et al., 2017; Burg, 2018; Sepidbar et al., 2020).

3. Methods

To provide a complete description of the Bajgan Complex, a field- and laboratory-based multidisciplinary study has been carried out. The field study included the geological mapping of selected key-areas, the lithological characterization and the mesoscale structural analyses. During the geological mapping, rock samples for different laboratory analyses has been collected. The laboratory study includes firstly the geochimical analyses of the meta-igneous rocks. In addition, the ages of the protoliths of the meta-igneous rocks have been determined by zircon U-Pb geochronology. The microscale features of the different deformation phases identified in the field have been analyzed in thin section. The metamorphism have been studied using different petrological thermobarometers in association to petrographic analyses that allowed a

reconstruction of a P-T path for the meta-sedimentary rocks. The dating of the main foliation has been performed by Ar-Ar geochronology on white mica. Finally, the emplacement age of post-metamorphic dykes has been constrained by zircon U-Pb geochronology in order to provide time constraints for final exhumation of the Bajgan Complex. Datailed informations are reported in the Supplementary Data 1. Mineral abbreviations are from Whitney and Evans (2010).

4. The Bajgan Complex

The Bajgan Complex (Figs. 2 and 3) is exposed in a triangular area of c. 2400 km^2. This area is bounded by the Sabzevaran Fault to the E, the Kanhuj-Nurabad line to the NW and the Rudan Thrust to the S. The Sabzevaran Fault and the Kanhuj-Nurabad line correspond to still active N-S trending dextral strike-slip faults, whereas the Rudan Thrust is an important km-thick brittle shear zone along which the Bajgan Complex is thrust onto the Sorkhband ophiolites and the Coloured Mélange (Delavari et al., 2016). The involvement of slices of *Nummulite*-bearing sandstones in the Rudan Thrust shear zone indicate its post-Middle Eocene age.

The Bajgan Complex consists of an assemblage of metamorphic rocks roughly aligned along a NW-SE and NE-SW trending main foliation and affected by NW-SE trending mylonitic shear zones. The Bajgan Complex is thus divided in different slices, each showing the same deformation history and the same metamorphic imprint. The main foliation and the shear zones are cut by swarm of not metamorphosed felsic dykes and covered by Quaternary continental deposits.

4.1. Lithostratigraphy

The Bajgan Complex shows a wide range of metamorphic rocks spanning from meta-serpentinites to meta-igneous and meta-sedimentary rocks (Fig. 4). The meta-serpentinites (Fig. 4a), mainly located in the northern area of the study area, are represented by huge bodies with massive fabric sorrounded by highly foliated zones. The massive meta-serpentinites generally preserves bands of chromitites as well as relics of the primary assemblage represented by pyroxene minerals. On the contrary, the foliated meta-serpentinites lack of relics of primary mineral assemblage and the foliation is represented by anastomozing slip surfaces where the serpentine group minerals are recrystallized.

The meta-igneous rocks are represented by both meta-volcanic and meta-intrusive rocks. The latter mainly consist of meta-gabbros with different mineralogical composition from gabbro, gabbronorite, melagabbro and anorthosite. The meta-gabbros are characterized by a strong strain partioning with a transition from poorly-deformed to foliated and mylonitic meta-gabbros. The poorly-deformed meta-gabbros show a well-preserved magmatic fabric with different grain-size and a magmatic layering due to different mineralogical composition and/or different grain size (Fig. 4b). In association with meta-gabbros, small stocks of meta-plagiogranites also occur (Fig. 4c). The foliated meta-gabbros are instead characterized by a metamorphic foliation and are affected by folding and boudinage. The mylonitic meta-gabbros are represented by fine-grained and strongly foliated rocks with rare porphyroclasts of magmatic pyroxene.

The meta-volcanic rocks occur as thick lenticular bodies of banded, well-foliated and lineated amphibolites. The bands consist of mm-scale amphibole- and plagioclase-rich layers, (Fig. 4 d). No magmatic relics have been identified in the meta-volcanic rocks.

The meta-sedimentary rocks include a thick package of meta-volcanoclastites, quarzites, micaschists, paragneisses, calcschists (all included in Micaschsist in Fig. 3) and impure marbles.

The meta-volcanoclastites corresponds to foliated epidote- and albite-rich schists sometime interlayered with mica-rich layers. The meta-volcanoclastites, in association with quarzites (Fig. 4e), are represented by quartz-rich layers alternanting with thin layers of well-foliated micaschists. The fine- to medium-grained impure marbles are instead composed of alternating layers of fine-grained marble and calcschists. In some locations, thick layers of fine- to medium-grained, well-foliated quartz-rich to quartz-free micaschists were documented probably at the top of impure marbles (Fig. 4f). The micaschists include thick fine-grained mica-rich layers and fine- to coarse-grained quartz-rich paragneisses.

The metamorphic rocks are cut by 1-2 m thick felsic dykes showing a good lateral continuity. The dykes are not metamorphosed and escape from the main deformation events detected in the Bajgan Complex. These dykes belong to the calk-alkaline magmatism that characterized the whole North Makran area during the Eocene (Burg, 2018).

4.2. Geochemistry of the magmatic protoliths

Twenty samples of metamorphic rocks derived from magmatic protoliths were selected for petrographic and whole rock geochemical studies with the aim of assessing their geochemical nature and the tectono-magmatic setting of formation. Analytical methods are given in Supplementary Data 1, whereas the analytical results are given in the Table 1, together with the key parameters for evaluating the quality of the data (i.e. accuracy and detection limits). Given the metamorphic nature of the studied rocks, only elements that are considered as immobile during alteration and metamorphic processes will be used in the following discussion. According to the geochemical features of the studied samples, three chemical Groups can be distinguished. Group 1 is composed by meta-cumulates, Group 2 includes meta-magmatic rocks showing

subalkaline nature (Nb/Y ratios <0.4), whereas Group 3 displays meta-magmatic rocks showing alkaline nature with Nb/Y ratios >1 (Fig. 5).

4.2.1. Cumulate rocks (Group 1)

The Group 1 is represented by meta-intrusive rocks whose compositions likely reflect an original mafic cumulate nature. This group includes one meta-anorthosite sample and a couple of meta-cumulate gabbros. The meta-anorthosite MK704 shows high SiO_2, Al_2O_3, CaO, Na_2O, P_2O_5, Ba, and Sr contents coupled with low contents in Th, Ta, Nb, TiO_2, and Y (Fig. 6a). Due to its cumulate nature, a definition of the magmatic affinity of this rocks cannot be straightforwardly determined. Nonetheless, the La (5 ppm), Ce (10 ppm), Th (0.2 ppm), Ta (0.14 ppm), and Nb (2 ppm) contents are low compared to those of anorthosites derived from enriched-type magmas (Mukherjee et al., 2005; Ghose et al., 2008; Shellnutt et al. 2020). Meta-cumulate gabbros MK254 and MK256 are characterized by high MgO contents (11.29-14.35 wt%) and Mg# (84-79), as well as by high values of compatible elements (e.g., Cr = 439-1069 ppm). By contrast, they show variable, but generally low abundances of incompatible elements. Th and Ta are about 1 time N-MORB composition (Sun and McDonough, 1989), whereas Nb, La, Ce, P, Nd, Zr, Ti, and Y are lower or much lower than N-MORB composition (Fig. 6a). The marked depletion of these samples suggests that the magmatic protolith of the meta-anorthosite and meta-cumulate gabbros were most likely formed from a MORB type parental liquid.

4.2.2. Subalkaline rocks (Group 2)

Based on the overal chemical composition, this group includes meta-gabbros, meta-plagiogranites, meta-basalts, and meta-ferrobasalts rock-types. Subalkaline rocks can be subdived, in turn, in two chemically distinct groups, which differ to each other for the content of

many trace elements and elemental ratios. The following description will be based to the distinguisched chemical groups rather than the rock types, as the aim of this study is to define the geochemical affinity of the meta-magmatic rocks.

The Group 2a is represented by one meta-gabbro, several meta-basalts and one meta-ferrobasalt. All these rocks display a clear sub-alkaline affinity, with Nb/Y ratio < 0.15 (Fig. 5). No significant chemical differences can be seen between the meta-gabbro MK705A and the meta-basalts, with the exception of relatively low TiO_2 (0.67 wt%) and high Cr (847 ppm) contents in sample MK705A. All these rocks show relatively high MgO (7.88-10.5 wt%) and compatible elements (e.g., Cr = 118-336 ppm) contents, as well as Mg# (69-60) coupled with generally low abundance of incompatible elements (e.g., TiO_2 = 1.28-1.44 wt%, P_2O_5 = 0.11-0.15 wt%, Zr = 80-109 ppm, Y = 27-40 ppm). The meta-ferrobasalt is characterized by very high TiO_2 (3.85 wt%), FeO_t (16.73 wt%), and V (453 ppm) coupled with low Mg# (54). Group 2a rocks show flat N-MORB normalized patterns with high field strength elements (HFSE) contents ranging from ~0.9 to ~1.6 times N-MORB abundance (Fig. 6b). These patterns are very similar to those observed in N-MOR basalts and gabbros (Sun and McDonough, 1989). An N-MORB affinity for this subgroup of rocks is further suggested by the discrimination diagrams in Figures 7a-c. In particular, these rocks plot in the field for subduction-unrelated settings, within the compositional field for typical N-MORB (Saccani, 2015). An N-MORB affinity is also suggested by the co-variation of Zr/Nb and Zr/Y ratios as shown in Figure 7d, in which these rock plot in the field for N-MORB compositions.

The second chemical group of subalkaline rocks (Group 2b) is represented by one meta-gabbro, one meta-plagiogranite, and some meta-basaltic rocks. This group of rocks display sub-alkaline affinity with, however, higher Nb/Y ratios (0.24-0.40) compared to Group 2a rocks (Fig. 5). No significant chemical differences can be observed between the meta-gabbro MK272 and meta-basalts; therefore, their composition will be described together. Group 2b mafic protoliths

show a small range of MgO (7.70-10.55 wt%) and Mg# (74-63). Though fairly variable, TiO_2 (0.88-1.61 wt%), P_2O_5 (0.09-0.31 wt%), Nb (6 -12 ppm), Y (15-31 ppm), and Zr (65-137 ppm) are generally high. Compatible elements contents are also variable, depending on the degree of fractionations of the different rocks and they show good positive correlations with MgO contents. The only exception is represented by the meta-gabbro MK272 in which Cr content (752 ppm) is fairly high in relation to the MgO value, possibly reflecting a small amount of Cr-spinel fractionation in the magmatic protolith. In the N-MORB normalized (Sun and McDonough, 1989) incompatible elements spider diagram, Group 2b meta-basalts and meta-gabbro show regularly decreasing patterns from Th (Th_N = ~5-~10) to Y (Y_N = ~0.5-~1) (Fig. 6c). These patterns are very similar to that of the typical enriched-type MORB (E-MORB) of Sun and McDonough (1989). In summary, the overall geochemical features of Group 2b meta-gabbro and meta-basalts point out for an E-MORB geochemical affinity of the magmatic protoliths, as also suggested by the diagrams in Figures 7a-d, where these rocks plot in the fields of typical E-MORB compositions (Wood, 1980, Cabanis and Lécolle, 1989; Sun and McDonough, 1989; Saccani, 2015). The meta-plagiogranite MK701A is characterized by high SiO_2 content (71.19 wt%) and very low contents of TiO_2, P_2O_5, MgO, Cr, Co, Ni. This rock show very high values of Y (115 ppm), Zr (374 ppm), Nb (35 ppm), Th (3.09 ppm), and Ta (1.71 ppm). The relatively high content in incompatible elements is exemplified in the N-MORB normalized incompatible elements pattern shown in Figure 6c. Significantly, this pattern is characterized by negative anomalies of Ti and P, which most likely reflect early crystallization and removal of Fe-Ti oxides and apatite during fractional crystallization. The crystallization of these minerals is indeed observed in differentiated melt with ferrobasaltic-andesitic compositions in MORB-type magmatic series (e.g., Beccaluva et al., 1983). The high Nb, Ta, Th, La, Ce, and Nd abundances, as well as a smootly decreasing pattern from Th to Y suggest that the magmatic protolith formed from a very fractionated melt most likely

derived, in turn, from an E-MORB type parental liquid. The Nb/Y ratio (Fig. 5) and the discrimination diagrams in Figure 7 strongly support the hypothesis of an E-MORB affinity for the meta-plagiogranite MK701A.

4.2.3. Alkaline rocks (Group 3)

The Group 3 includes five meta-basalts, which show alkaline affinity, as suggested by the high (i.e., > 1.1) Nb/Y ratio (Fig. 5). Group 3 meta-basalts display rather homogeneous compositions. MgO contents are in the range 7.30-10.90 wt% and Mg# is generally around 60, with the only exception of sample MK247 (MgO = 7.30 wt%) that has Mg# = 53, likely suggesting a moderately fractionated nature. TiO_2 (1.84-2.33 wt%) and P_2O_5 (0.16-0.56 wt%) contents are relatively high, in agreement with the alkaline affinity of these rocks and generally higher than those of Groups 2a and Group 2b rocks. Accordingly, these rocks show higher contents of Nb (24-68 ppm) and Zr (148-214 ppm) compared to the other groups, whereas Y (21-37 ppm) abundance is comparable with that of Group 2b rocks. Quite different contents of Cr (66-350 ppm) and Ni (27-141 ppm) are observed in the Group 3 rocks. The incompatible elements spider diagrams are characterized by marked enrichment in large ion lithophile element (LILE) with respect to HFSE and show regularly decreasing patterns from Rb to Y (Fig. 6d). Significantly, these patterns are well comparable with those of ocean island basalt (OIB)-type basalts (Sun and McDonough, 1989). Accordingly, in the tectonic discrimination diagrams in Figures 7a-c, Group 3 rocks plot in the field for subduction-unrelated settings, namely within the compositional fields for typical P-MORB and OIB. A similar conclusion can be found out from the Zr/Nb vs. Zr/Y diagram (Fig. 7d) in which the rocks of Group 3 plot close to the composition of the typical OIB (Sun and McDonough, 1989).

4.3. Deformation history

According to the overprinting relationships detected in the field, four deformation phases, namely D1, D2, D3, and D4, were recognized in the Bajgan Complex. The first deformation phase (D1) was occasionally documented as relics of a S1 continuous foliation and as scattered isoclinal F1 folds at both the meso- and microscopic scale. The D2 phase produced the main strucures documented in the field (Fig. 8a). It developed under a strong strain partitioning regime that results in several slices recording F2 folds and S2 axial plane foliation (folding domains), bounded by D2 shear zones (shearing domains) generally localized at the boundaries between the different litotypes and showing a top to the S-SW sense of shear. In both domains, the S2 foliation (i.e., the main foliation documented in the field) is mostly oriented from NW-SE to E-W with variable dip, mainly toward E (Fig. 9).

The S2 axial plane foliation is a continuous and pervasive foliation (Fig. 8b and c) that bears a L2 mineralogical lineation represented by elongated grains of quartz, calcite and amphibole showing variable orientation from NE-SW to NNW-SSE with variable plunge (Fig. 9). Tight to isoclinal F2 folds are well developed within meta-volcanoclastics (Fig. 8b and c), fine-grained micaschists and fine-grained paragneisses. The F2 folds show symmetric profile with thickened hinge, thinned and delaminated limbs and sub-rounded up to sub-angular hinge profile (Fig. 8). A2 fold axes mostly trends from NW-SE to NE-SW with a plunge mainly ranging from 0 to 40° (Fig. 9).

The third deformation phase (D3) is mainly represented by cylindrical F3 folds (Fig. 8c and d) showing interlimb angle ranging from 30° to 120° and sub-angular to sub-rounded hinge zones. The $L_{(S2\text{-}S3)}$ intersection lineation is mainly represented by the intersection of S3 foliation-S0 bedding and mullion structures. A3 fold axes trend mainly from NW-SE to NE-SW with low-angle

plunge (Fig. 9). S3 foliation is a spaced axial plane crenulation cleavage that in the most competent lithology can be classified as disjunctive foliation. In the whole Bajgan Complex, the S3 foliation is characterized by a low-angle attitude (Fig. 9). No evidence of mineralogical lineation has been detected on the S3 foliation. F3 folds are associated with NW-SE-trending extensional shear zones dipping from 20° to 60° toward north and showing a top-to-the S sense of shear.

The fourth deformation phase (D4) produced open to gentle and upright folds with rounded hinges and A4 axes trending from W-E to NW-SE. The axial plane foliation S4 is a disjunctive cleavage without sin-kinematic recrystallizations that show a NE-SW strike and subvertical dip. It is important to outline that the felsic dykes cut the foliations developed during the D1, D2 and D3 phases as well as the shear zones that subdivide the Bajgan Complex into several slices. However, these dykes are deformed by the D4 phase folds. Finally, high-angles dextral strike-slip or oblique faults probably belonging to the Sabzevaran Fault system dissect all the structures of the Bajgan Complex.

4.4. Microstructural features

The meta-serpentinites have a mylonitic to ultramylonitic fabric with the S2 mylonitic foliation marked by chlorite + serpentine + opaque minerals that wraps rounded aggregates of serpentine and/or pale green Amp and olivine crystals. Occasionally in low strain domains, relicts of protoliths texture (e.g., porphyroclast of clinopyroxene, olivine and red-brown spinel) were documented.

In the meta-gabbros, the S2 foliation is a continuous foliation marked by layers of green to pale blue elongated amphibole crystals (100-200 μm) ± quartz ± feldspar ± epidote ± opaque

minerals (Fig. 10a) and/or by 1-2 mm thick layers of very fine-grained green amphibole + opaque minerals. These layers wraps very large brown amphibole crystals (1-5 mm) affected by undulatory extinction, irregular boundaries, and folding. Within the D2 shear zones, the large feldspar grains showing weak shape preferred orientation, asymmetric tails of small syn-kynematic green amphibole + epidote, bookshelf structures, and locally fishoid shape. All these features are coherent with the same sense of shear. Quartz show lobate grain boundary suggesting that dynamic recrystallization occurred by grain boundary migration mechanism.

In the meta-plagiogranites, the S2 foliation is marked by quartz + phengite + chlorite + epidote ± albite ± garnet ± green amphibole ± clorithoid ± opauq minerals wrapping mm-sized feldspar crystals showing weak undulatory extinction, lobate boundary, rare deformation twins, and a variable grade of recrystallization. Quartz shows strong crystal preferred orientation, weak undulatory extinction and dragging structures and lobate grain boundary indicative of grain boundary migration recrystallization. This fabric is partly overprinted by grain boundary area reduction mechanisms that produced straight boundaries and 120° triple points. Large (400-700 μm) white mica crystals are folded and show evidence of undulatory extinction.

In meta-volcanic rocks, the S2 foliation is highlighted by a mm-thick layers of green amphibole + chlorite ± opaque minerals, and fine-grained quartz + albite + epidote ± calcite locally wrapping coarse-grained Pl porphyroclasts. In meta-volcanoclastites and in micaschists, relicts of S1 foliation are preserved in the hinge zones of F1 folds (Fig. 10b) and as aggregates of chlorite + white mica crystals oriented orthogonal to the S2 foliation (Fig. 10c). In micaschists, the S2 foliation is marked by a compositional layering consisting of quartz + phengite + feldspar ± garnet ± epidote (Fig. 10c, d), and phengite + chlorite. Quartz grains shows weak undulatory extinction, moderate to weak shape preferred orientation and locally, dragging structures (Passchier and Trouw, 2005), lobate boundaries and seriate grain size (Fig. 10c). These features

may suggest that recovery involved both subgrain rotation and grain boundary migration recrystallization. Quartz often has polygonal grains and straight grain boundaries that meet in 120° triple points indicating that grain boundary area-reduction mechanisms locally occur (Fig. 10c, d). Locally, feldspar have thin deformation twins (Fig. 10d) and a thin and irregular ribbon of feldspar neoblasts. Garnets are euhedral, 150-200 μm in size with homogeneous composition and no evidence of replacing (Fig. 10e). These features suggest that they grew simultaneously to the development of the S2 foliation. These layers wrap feldspar crystals (400-700 μm) showing lobate grain boundaries, weak undulatory extinction and a strong shape preferred orientation. D2 shear zones (Fig. 10e) are highlighted by less than 1 cm-thick S-C-C' structures and σ-type porphyroclasts of feldspar crystals with asymmetric tails of chlorite + phengite + fine grained quartz ± Ep in micaschists. C and C' planes are highlighted by phengite + fine grained quartz.

In impure marble, the S2 foliation is mainly highlighted by mm- to cm- thick layers of calcite ± green amphibole ± chlorite ± quartz (Fig. 10f). Calcite crystals locally show thick and irregular deformation twins (i.e., Type IV of Ferrill et al., 2004) (Fig. 10g). Quartz shows lobate grain boundaries, seriate grain size, well-defined crystal preferred orientation, and weak undulatory extinction. Evidences of the old S1 foliation is highlighted by chlorite crystals oriented at high angle respect to the S2 foliation.

At the microscopic scale, the S3 foliation is well-developed in the micaschists and fine-grained paragneisses where consists of rough to smooth cleavage domains mainly highlighted by thin films of opaque minerals and oxides along dissolution surfaces (Fig. 10h). Dissolution processes and rigid body rotation of small pre-existing minerals are the main mechanisms of S3 foliation development. The S4 axial plane foliation is represented by a spaced, disjunctive cleavage, mainly recognized in the F4 folds hinge zones.

4.5. Petrological thermobarometers

The detailed microscale study presented above allow to chose the suitable rock types to estimate the P-T conditions for the different deformation phases. The microstructures and the metamorphic recrystallization observed in the micaschists indicate that this rock type is the best samples to estimate the P-T conditions of the D1 and D2 phases, as the relationships of the S1 relics and S2 foliation can be recognized. Selected samples of micaschist have been collected in different slices and three samples (MK701B, MK706 and MK707) have been chosen as representative. The mineral chemistry of selected phases of these samples is provided in Tables 1S2, 2S2 and 3S2 of the Supplementary Data 2. Temperature and pressure conditions were estimated using the chlorite-quartz-water (Vidal et al., 2006) and the phengite-quartz-water (Dubacq et al., 2010) methods, respectively (Table 1S1 of the Supplementary Data 1). The results of these two methods allowed to identify different areas in the P-T space representing the stability fields of the D1 and the D2 phases. The chlorite and phengite analysis employed for these calculations were also used to calculate the equilibria of single chlorite-phengite couples through the chlorite-phengite-quartz-water method (Vidal and Parra, 2000). In the sample (MK 701B) in which the chlorite and the phengite phases were not present, the pressure conditions were instead calculated using the Al-in hornblende barometer (Schmidt, 1992).

4.5.1 Chlorite-quartz-water method

This method (Vidal et al., 2006) was applied on samples MK707 (see Supplementary Data 2) and MK706. In the sample MK707 the calculations were performed fixing pressures at 0.60 GPa and water activity at 0.8. The single generation of chlorite identified in this sample (chlorite D2, see Supplementary Data 2), turns out to be stable in a T range of 280-450°C. In the sample

MK706 three selected groups of chlorite were distinguished: the first group (chlorite D1) were sampled within the S1 foliation and shows a composition enriched in daphnite end-member (see Supplementary Data 2). The second (chlorite early-D2) and the third (chlorite late-D2) groups are related to the S2 foliation and show a predominance of amesite and sudoite end-members, respectively (see Supplementary Data 2). The calculations were performed fixing pressures (0.60 GPa, 1.20 GPa and 0.40 GPa for the first, second and third groups respectively) and water activity (0.8) parameters. The T ranges of stability calculated are 150-320°C and 375-400°C for chlorite D1 (Fig. 11a), 250-330°C and 370-450°C for the chlorite early-D2 (Fig. 11b), and 150-350°C and 375-400°C for the chlorite late-D2 (Fig. 11c).

4.5.2 Phengite-quartz-water method

This method (Dubacq et al., 2010) was used to calculate the P ranges through the Ph compositions. In the sample MK707, one generation of phengite developed parallel to the S2 foliation (phengite D2) were analyzed (see Supplementary Data 2). The calculations were performed within the T range obtained with the chlorite-quartz-water method (i.e. 280-450°C), and the % Fe^{3+} to 30, which results to be the best optimized value. All the calculations with the phengite-quartz-water method have been performed fixing the water activity to 0.8. The P estimate for the D2 phase of sample MK707 ranges between 0.40 and 1.00 GPa. The phengite observed in the sample MK706 have been divided into three groups: phengite grown along the S1 foliation (phengite D1) that shows a pyrophyllite affinity and the phengite grown along the S2 foliation, distinguishing those enriched in the celadonite end-member (phengite early-D2) from those wth Ms predominance (phengite late-D2, see Supplementary Data 2). To apply the phengite -quartz-water method, different T ranges of stability has been assigned to the three groups of phengite on the base of the chlorite-quartz-water method's results (i.e., the T range of

chlorite D1 for the phengite D1, those of chlorite early-D2 for the phengite early-D2 and those of chlorite late-D2 for the phengite late-D2), as well as the % Fe^{3+} content. All the calculations with the phengite -quartz-water method have been performed fixing the water activity to 0.8. The results show different P ranges for the different groups of phengite ; in detail, the P range associated to the phengite D1 is 0.33-0.96 GPa, whereas the P range of phengite D2 are: 0.60-1.35 GPa for phengite early-D2 and 0.22-0.78 GPa for the phengite late-D2 (Fig. 11).

4.5.3 Al-in-hornblende barometer

The estimation of the P condition of the sample MK701B was performed through the calibration based on the Al_{tot} content in calcic amphibole following Schmidt (1992) (Fig. 12). The analyzed Ca-amphibole belong to the metamorphic paragenesis, which constitute the main S2 foliation (see Supplementary Data 2). Therefore the P range calculated for the sample MK701B of 0.80-1.10 GPa regards the P condition registered during the early D2 phase (Fig. 12).

4.5.4 Chlorite-phengite-quartz-water method

After the identification of the chlorite-phengite pairs within the same microstructure, this method (Vidal and Parra, 2000) allows to find points in the P-T space, which represent their optimized equilibrium conditions in presence of quartz and water. We applied this method only to selected chlorite-phengite couples that reach the equilibrium in the T and P ranges calculated with the chlorite-quartz-water and phengite-quartz-water methods. Sample MK707 is characterized by a single population of chlorite and phengite (chlorite-phengite D2) that reached the equilibrium condition at 0.60-1.00 GPa and 280-320°C (see Supplementary Data 2). In the sample MK706 the equilibrium conditions related to the first generation of chlorite and phengite (chlorite-phengite D1) are 0.52-0.94 GPa and 250-295°C, those related to the second generation

(chlorite-phengite early-D2) are 1.05-1.30 GPa and 260-310°C and those related to the third generation (chlorite-phengite late-D2) are 0.28-0.57 GPa, 315-350°C (Fig. 11). The P-T conditions calculated with the chlorite-quartz-water, phengite-quartz-water and chlorite-phengite-quartz-water methods of the sample MK706 were compared with those estimated with classical thermobarometry (see Supplementary Data 2).

4.6. Microstructure-based thermometers

In order to achieve a complete view on the tectono-metamorphic history of the Bajgan Complex, the P and T estimates deduced by petrological thermobarometers have been integrated by microstructure-based thermometers. The results mainly concern the D2 phase, i.e. the most pervasive deformation detected in the field and in thin section. T conditions were estimated using quartz and calcite microstructures.

4.6.1 Quartz microstructures

Quartz microstructures were mainly documentedin quartz-rich layers parallel to S2 foliation within the meta-plagiogranites as well as within the paragneisses and quartz-rich micaschists. quartz microstructures (Fig. 10c, d) documented on these lithologies (i.e., weak undulatory extinction, lobate boundary, dragging structures) suggest deformation temperature of at least about 450-500°C. Analogous deformation temperature can be deduced by the microstructure documented on feldspar crystals (i.e., undulatory extinction, lobate boundary, rare deformation twins, recrystallization and the lack of microfaulting). Microstructures on the larger porphyroclasts of white mica suggest medium grade deformation temperature.

4.6.2 Calcite microstructures

The calcite microstructures have been studied in the impure marble, where levels of calcite are aligned along the S2 main foliation. The thick and irregular deformation twins documented on calcite crystals (Fig. 10g) indicate that during the late-D2 event, part of the deformation was accommodated also by dynamic recrystallization. Using the geothermometer proposed by Ferrill et al. (2004), this twin geometry indicates temperature >250°C. Since above T = 400°C in calcite crystal plastic-deformation is mainly accommodated by dynamic recrystallization, we can roughly constrain the deformation temperature obtained by calcite geothermometer between 250 and 400°C.

4.7.U-Pb geochronology of the meta-intrusive rocks

Three samples of meta-intrusive rocks have been collected to achieve reliable ages of protoliths crystallization by zircon U-Pb geochronology. These rocks correspond to the meta-plagiogranite MK701A (E-MORB affinity), the meta-anorthosite MK704 (Subalkaline affinity), and the meta-gabbro MK705A (N-MORB affinity). These samples have been collected in different slices of the Bajgan Complex with the aim to obtain a complete picture of the ages for the meta-intrusive rocks. Zircon grains from the three sample have been separated and analyzed (see Supplementary Data 1).

Large part of the U-Pb data from zircon from samples MK704 and MK701A resulted severely discordant (Table 2). The zircon grains from sample MK701A are generally euhedral and small (<100μm) with low aspect ratios (Fig. 13). They are characterized by large homogeneous core surrounded by a brighter thin rim and rarely a faint oscillatory zoning is recognisable. Inclusions of Ap are common (cathodoluminescence (CL) features of: zrc55, 67, 50, 52 see Fig.

13). Nineteen U-Pb analyses on seventeen zircon grains were collected for the MK701A sample. Only 7 data provided a concordance <8% (Fig. 13) and a weighted average $^{206}Pb/^{238}U$ age of 156±6Ma.

The zircon grains from sample MK704 are generally small (<75μm) and stubby (Fig. 13). They are characterised by darker core surrounded by brighter rims (zircons 87, 88, 92, 104 see Fig. 13). Thirteen U-Pb analyses on fifteen zircon grains were performed for sample MK704. Nine U-Pb ratios with a concordance <9% provided a weighted average $^{206}Pb/^{238}U$ age of 136±3Ma (Fig. 13).

The zircon grains from sample MK705 are euhedral, small (<100μm) and with low aspect ratios (Fig. 13). Oscillatory zoning can be observed in Zrc78, whereas Zrc72, 76, and 83 are characterized by homogeneous large cores. These zircon may contain inclusions of AP. Twelve U-Pb analyses on eleven zircon grains were collected for sample MK705. U-Pb data showed a concordance better than those observed within other samples, generally <2%, with a weighted average $^{206}Pb/^{238}U$ age of eight data at 112±4Ma (Fig. 13). Overall, the obtained crystallization ages for the meta-intrusive rocks from the Bajgan Complex range from 156±6Ma to 112±4Ma (i.e., from Late Jurassic up Early Cretaceous) (Fig. 13).

4.8. U-Pb geochronology of the felsic dyke

To constrain the young age limits of the main deformation and metamorphism phases, a sample (MK328B) of a not metamorphosed felsic dyke has been collected for zircon dating. Only a few zircon grains and crystal fragments were recovered from the dyke and just one euhedral crystals was analysed (Table 3). The selected zircon was prismatic with a length of ~ 250 μm and an aspect ratios (i.e. length/width) of 3:1. The U-Pb age of this crystal was determined by

chemical abrasion isotope-dilution thermal ionization mass spectrometry (CA-ID-TIMS) at the University of Geneva (Switzerland). The zircon $^{206}Pb/^{238}U$ date was corrected for initial ^{230}Th-^{238}U disequilibrium (Schoene, 2014) as described in the Supplementary Data 1. The crystals gave a concordant and extremely precise $^{206}Pb/^{238}U$ age of 41.99 ± 0.07 Ma (uncertainty expressed as 2σ), which is interpreted as the age of emplacement of the leucocratic dyke.

4.9. Ar-Ar- geochronology of the micaschists

Three samples of micaschists (MK463, MK706, and MK707) have been collected for the mica Ar-Ar geochronology. To constrain the age of metamorphism, we performed ^{40}Ar-^{39}Ar step-heating analysis on metamorphic white mica that have been separated from the collected samples (see Supplementary Data 1 for detail on analytical method). In the three samples, the main S2 foliation is marked by white mica + chlorite-rich layers wrapping granoblastic layers of quartz + feldspar ± calcite. Large white mica (125-250 μm) separates gave lowermost Late Cretaceous ages ranging from c. 100 to c. 91 Ma (Cenomanian to Turonian) (Fig. 14). In detail, ^{40}Ar-^{39}Ar white mica plateau age (Fig. 14) is constrained at 93.75±0.85Ma and 93.55±0.84 Ma for sample MK463, at 91.30±0.78 Ma and 91.23±0.74 Ma for sample MK706, and at 100.11±0.98 Ma and 100.10±0.92 Ma for sample MK707 (see Supplementary Data 1).

5. Discussion

5.1. The Bajgan Complex re-interpreted as remnant of a Late Jurassic-Early Cretaceous oceanic lithosphere

Results from the present study demonstrate that the so far proposed interpretations for the Bajgan Complex as the pre-Mesozoic continental basement of a microcontinent, i.e., the so-called Bajgan-Durkan microcontinent (McCall, 1985; Hunziker et al., 2015; Burg, 2018; Saccani et al., 2018), must be completely revalued. In fact, several lines of evidence suggest that the Bajgan Complex consists of the remnants of a Late Jurassic-Early Cretaceous oceanic lithosphere.

The first line of evidence is provided by the presence of meta-igneous rocks, whose geochemistry can be used to constrain their geodynamic setting of origin (Saccani 2015 and quoted references). According to the geochemical data, the magmatic protoliths of the Bajgan Complex include meta-cumulate (Group 1), subalkaline (Group 2), and alkaline (Group 3) rocks (see Pearce, 2008, Dilek and Furnes, 2011; Saccani, 2015). Mafic cumulate protoliths (Group 1a) show a general MORB affinity. Their chemical composition is strongly influenced by cumulus processes and therefore we cannot exactly define whether they derived from normal or enriched types MORB melts. In contrast, volcanic and gabbroic protoliths range from N-MORB (Group 2a) to E-MORB (Group 2b) and OIB (Group 3) chemical compositions (Figs. 6 and 7). These rocks show different incompatible trace elements ratios, which point out for different compositions of their mantle sources (Allègre and Minster, 1978; Pearce, 2008; Saccani, 2015). The co-variation of Zr/Nb vs. Zr/Y show that the different rocks plot along the mixing line between the N-MORB and OIB end member compositions (Fig. 7d). This suggests that the Group 2a volcanic protoliths were derived from sub-oceanic depleted mantle sources, whereas the weakly enriched Group 2b rocks and the enriched Group 3 protoliths record variable influence of plume–type components on the sub-oceanic depleted mantle (plume-ridge interaction). The meta-igneous rocks have been thus formed within distinct tectono-magmatic settings within a subduction-unrelated oceanic basin. These settings include mid-ocean ridge (for Group 2 rocks) and within-plate seamounts (for Group 3 rocks), suggesting a polygenetic MORB and OIB crust within the oceanic basin from

which the meta-ophiolites of Bajgan Complex derived.

The second line of evidence is represented by the magmatic age of the meta-intrusive rocks that has been determined by zircon U-Pb geochronology. The age ranges from 156 to 112 Ma, i.e., from Oxfordian to Aptian. These data exclude a Paleozoic origin for the protoliths of the meta-igneous rocks of the Bajgan Complex. As this complex is composed by different tectonic slices, this rather wide age range most likely suggest that the different slices correspond to distinct meta-ophiolites derived from different segments of the same Mesozoic oceanic basins. This wide age range coupled with the geochemical characteristics of the meta-igneous rocks of the Bajgan meta-ophiolites imply that this Mesozoic oceanic basin was characterized by a well-developed and thick oceanic lithosphere that developed for a long time (more than 40 Ma) and produced MOR-type intrusive and effusive rocks. The presence of OIB and E-MOR meta-basalts also point to a plume influenced magmatism in this Mesozoic Basin (cfr. plume proximal oceanic lithosphere of Pearce, 2008).

The third line of evidence is provided by the lithostratigraphy. In fact, the Bajgan Complex represents an assemblage of slices that are composed by both subduction-unrelated meta-ophiolites and meta-sedimentary rocks. In this framework, the meta-serpentinites in the Bajgan Complex can be interpreted as remnants of the upper mantle section of the subducting oceanic slab. The various types of meta-intrusive rocks from the Bajgan Complex were likely derived from metamorphism and deformation of a primary sequence of gabbro, gabbronorite, melagabbro and anortosite but also including more felsic rocks such as plagiogranites. This sequence can thus be interpreted as the remnants of the intrusive portion of typical subduction-unrelated ophiolites (Dilek and Furnes, 2011). The meta-volcanic rocks from the Bajgan Complex likely derived from the metamorphism of massive and/or pillow-lava basalts and can be interpreted as the volcanic sequence of the upper part of the oceanic crust. Associated to meta-volcanic rocks, the

widespread meta-volcanoclastics are representing the transition to the meta-sedimentary rocks. The meta-sedimentary rocks derive from a pristine deep-sea, pelagic succession including cherts, limestone and siliciclastic to mixed turbidites. All these lithologies are generally found in the sedimentary deposits at the top of the oceanic crust in subduction-unrelated oceanic basin. The age of this assemblage cannot be detected by fossils because they have been totally recrystallized during the metamorphism, but an Early Cretaceous age can be proposed according to the Late Jurassic-Early Cretaceous age of meta-igneous rocks and the Late Cretaceous age of the metamorphism. It is worth to note that no metamorphic rocks clearly derived from continental crust, such as meta-granites, meta-rhyolites, meta-conglomerates or meta-dolostones, have been detected during the field survey. Therefore, the lithostratigraphy of the Bajgan Complex is coherent with its origin from deformation and metamorphism of Late Jurassic – Early Cretaceous oceanic lithosphere.

5.2. The tectono-metamorphic history of the Bajgan Complex

The interpretation of the Bajgan Complex as a Late Jurassic-Early Cretaceous meta-ophiolites is confirmed by the tectono-metamorphic evolution reconstructed in the meta-sedimentary rocks. As previously described, the Bajgan Complex is represented by an assemblage of slices, each bounded by mylonitic shear zones developed during the D2 phase. In each slice, the same polyphase deformation history from D1 to D3 phases has been reconstructed. The significance of these phases is discussed in this section taking into account the P-T conditions estimated for the metamorphic mineral assemblage grew along the S1 (section 5.3.1) and S2 (section 5.3.2) foliations. These estimates are here discussed using the results of both the

petrological- and microstructure-based thermobarometer described in sections 4.5 and 4.6, respectively.

The relics of the D1 phase have been identified in several samples. In the studied sample P and T estimates by chlorite-quartz- water and chlorite-phengite-quartz-water methods indicate that D1 phase were acquired during blueschist facies conditions (T = 250-295°C, P = 0.52-0.94 GPa) at depth of c. 17-31 km (Fig. 15). Even if the available data do not allow a detailed reconstruction of the D1 metamorphic history for the whole Bajgan Complex, the identification of the high-pressure metamorphism represents a useful constraint for the interpretation of the D1 phase.

More data are instead available for the D2 phase. The data acquired by the thermodynamic calculations conducted by chlorite-quartz-water, phengite-quartz-water, and chlorite-phengite-quartz-water methods indicate the occurrence of two groups of mineral assemblage grown along the S2 main foliation. In detail, the first group of minerals is grown during the early stage of D2 phase, whereas the second group of minerals is grown during the late stage of D2 phase. P and T conditions for the first group of minerals can be framed between 0.30-1.35 GPa and 250-450°C. These metamorphic conditions can be further constrained by Al-in-hornblende method that indicates a P of 0.80-1.10 GPa for the early stage of the D2 phase. In addition, the quartz microstructures suggest a T during the deformation at least of 450-500°C. These values are in contrast with the petrology-based thermometer that indicate maximum temperature of 450°C. However, this is an apparent contradiction biased by the fact that: (1) quartz microstructures are sensitive to other variables such as strain rate and hydrolytic weakening (see review by Law, 2014) and (2) microstructures-based geothermometer, as defined by Tullis (2002), is a precise combination of strain rate/temperature/water content. Experimental results demonstrate that a small increase in water content is equivalent to an increase of c. 100°C

in deformation temperature (Law, 2014 and references therein). Considering the geodynamic environment, is reasonable to assume a relevant addition of trace amounts of water released during the compaction of the oceanic sediments during the deformation. In conclusion, microstructures-based thermometer provides 'apparent' higher deformation temperature. Consequently, the T during early stage of D2 phase can be estimated as c. 450°C according to results of the combination of petrological- and microstructural-based geothermobarometer. To summarize, the P and T conditions during the early stage of the D2 phase occur at T c. 450°C and P=0.80-1.10 GPa corresponding to the boundary between blueschist and epidote amphibolite metamorphic facies (Fig. 15).

The thermodynamic calculations conducted by chlorite-quartz-water, phengite-quartz-water, and chlorite-phengite-quartz-water methods onto the second group of minerals have returned a wide range of P and T conditions (i.e., 0.22-0.78 GPa and 150-400°C). The data acquired from the microstructure of calcite twinning indicate a T higher than 250°C. The combination of petrological- and microstructure-based thermobarometer, thus, constrains the P and T conditions of the late stage of the D2 phase within the greenschist metamorphic facies. This result is also suggested by combining the result of the chlorite-phengite-quartz- water multi-equilibrium approach (Vidal and Parra, 2000) and chlorite-quartz- water method (Vidal et al., 2006) that indicate P and T conditions of 0.28-0.57 GPa and 315-350°C (Fig. 15).

5.3. The Bajgan Complex record underplating-exhumation path in a Cretaceous subduction complex

To summarize, the combination of petrological- and microstructure-base geothermobarometers indicate that the D1 phase was developed at T and P corresponding to

blueschist metamorphic facies conditions. During the D2 phase two different mineral assemblages were registered. The early stage of the D2 phase occurs at T and P corresponding to the boundary between blueschist and epidote amphibolite metamorphic facies conditions. The late stage of the D2 phase instead occurs at T and P corresponding to greenschist metamorphic facies conditions (Fig. 15).

A first constraint is provided by zircon U-Pb geochronology that indicate an age of the meta-intrusive rocks ranging from Oxfordian to Aptian, thus suggesting an inception of subduction almost after the boundary between Early and Late Cretaceous. A further important constraint for the significance of the metamorphic evolution of the Bajgan Complex is also provided by the age of the D2 phase that has been determined using Ar-Ar dating on white mica grown along the D2 foliation. These data indicate that D2 event occurred during the Cenomanian-Turonian (100-90 Ma). The Ar-Ar white mica closure temperature of c. 350°C (Hodges, 1991) support the interpretation that this radiometric age can be developed during the D2 phase. Furthermore, these age constraints agree with the findings of Late Cretaceous HP-LT metamorphic rocks from the Coloured Mélange in the northeastern North Makran (i.e., Iranshahr area, Bröcker et al., 2021).

The sequence of deformation phases, from D1 to D3, coupled with the P-T conditions of the metamorphism that shows a clockwise trajectory from blueschist to greenschist facies (Fig. 15), is coherent with a transfer of fragments of oceanic lithosphere at the base of an accretionary wedge and their subsequent exhumation up to shallow structural levels (Platt, 1986; Cloos and Shreve, 1988; Scholl and von Huene, 2007; Meneghini et al., 2009; Agard et al., 2018; Ruh, 2020). The D1 phase thus resulted from the coherent underplating of slices of oceanic lithosphere at the base of an accretionary wedge within a subduction zone. The interpretation of the early stage of the D2 phase is more puzzling. Even if more data are required for the interpretation of the

early stage of the D2 phase, its development occurs after the underplating at the same depth or slightly deeper than D1 phase but during an increase of T. The early stage of the D2 phase can be thus regarded as a post-underplating deformation probably acquired within the subduction channel (i.e., the wedge-shaped zone at the interface between the down-going plate and the accretionary wedge). The subduction channel is the site of the exhumation of high- and ultrahigh-pressure metamorphic slices up to shallow crustal levels, and eventually to the surface, from depths of more than 100 km. However, the subduction channel is characterized by complex dynamics that produced a flow of the underplated material not only upwards but also downwards, and always in presence of ductile deformations (e.g., Platt et al., 2018). The early stage of the D2 phase possibly represent a tectono-metamorphic event occurred within the subduction channel after the underplating. Consequently, the deformations related to the late stage of the D2 phase can be regarded as acquired when the process of the exhumation was in an advanced stage, as indicate by the strong decrease of P condition, coherent with a depth of 9-19 Km (Fig. 15). The exhumation continued also during the D3 phase, when semi-brittle to brittle deformations developed probably at very shallow levels.

Our study can be compared with that provided by Dorani et al. (2017) that indicate a T during the main deformation of the Bajgan Complex higher than that established in this paper. Probably, this difference in the T value is detected in two different slices that experienced deformation at different T conditions through time. In a subduction setting, the thermal regime can in fact change in response to geodynamic events like a subduction of an oceanic seamount or a decrease in the convergence rate (e.g., Peacock, 1996; Syracuse et al., 2010: Frassi et al., 2020).

This tectono-metamorphic history of the Bajgan Complex is analogous to that reconstructed for the oceanic lithosphere in many world-wide fossil accretionary wedges

(Marroni et al., 2004; Guillot et al., 2009; Fagereng and Cooper, 2010; Plunder et al., 2015; Schmidt and Platt, 2018; Meneghini et al., 2020; O'Brien and Grove, 2020) where the deformations acquired during the accretion are followed by those developed during the exhumation. The latter resulted into the transfer of the meta-ophiolites and related meta-sedimentary deposits from the deep in the accretionary wedge up to shallow structural levels.

To sum up, the Bajgan Complex experienced burial and underplating reaching the blueschist facies metamorphism conditions and then exhumation from deep to shallow crustal levels. This evolution is constrained by the emplacement of the Middle Eocene (41.95 ± 0.07 Ma) felsic dykes that escape from the deformations related to D1, D2, and D3 phases, but are affected by the D4 phase, as indicated by brittle deformation of the phenocrystals. These dykes can be related to the widespread calk-alkaline magmatic activity found in the whole North Makran area (Burg, 2018). The age of the dykes thus indicates that the Bajgan Complex was exhumed from c. 30 km to shallow level in the time spam from c. 90-101 Ma to c. 42 Ma.

5.4. Implications for the geodynamic history of the Makran region

Most of the so far proposed reconstructions for the geodynamic history of the Makran area are based on the occurrence since the Early Cretaceous of two different oceanic basins, namely the North Makran basin located close to the continental margin of Lut Block and the wide Neo-Tethyan basin, whose remnant is still subducting. These two basins are interpreted as developed in different geodynamic settings with different times and affected by different geodynamic evolutions. The North Makran Oceanic basin is regarded as opened in a supra-subduction setting in the Late Jurassic-Early Cretaceous and completely closed before the Eocene, according to the occurrence of Early Eocene sedimentary deposits unconformably lying

at the top of the tectonic units derived from the North Makran basin. The location of these tectonic units north of the present-day subduction zone suggest a pristine location of the North Makran Oceanic basin between the margin of the Lut Block and a microcontinent, the so-called Bajgan-Durkan microcontinent. The proofs of the existence of this microcontinent are searched in two different units of North Makran, i.e., the Durkan and the Bajgan Complexes. The former has been regarded as consisting of a highly deformed assemblage mainly consisting of shallow water deposits associated to abundant volcanic rocks (McCall, 1985; Hunziker, et al., 2015). This complex has been commonly interpreted as the sedimentary cover of the Bajgan Complex that is regarded as a continental basement older than Paleozoic (e.g., McCall and Kidd, 1982; Samimi Namin, 1983; McCall, 1985; Hunziker, et al., 2015; Burg, 2018). This reconstruction must be modified according to the evidence provided by Barbero et al. (2021a,b) and by this paper. The data provided by Barbero et al. (2021a,b) indicate that the Durkan Complex represents fragments of seamounts tectonically incorporated in the Makran accretionary wedge during the latest Late Cretaceous-Paleocene. In addition, in this paper we provided evidences that the Bajgan Complex cannot be regarded as a continental basement of Paleozoic age but instead it represents a Cretaceous accretionary wedge involving Late Jurassic – Early Cretaceous ophiolites.

Thus, the mechanism of closure for the North Makran oceanic basin by a collision of a microcontinent with the margin of the Lut Block seems to be unlikely and different geodynamic mechanism must be proposed. A valuable suggestion is provided by the occurrence of the remnants of volcanic seamounts in the North Makran. These remnants are preserved within the Durkan Complex (Barbero et al., 2021a,b), but also in the Band-e-Zeyarat ophiolites where the remnants of an Early Cretaceous oceanic crust formed in a mid-ocean ridge setting and variably metasomatized by plume-type components has been testified by Barbero et al. (2020b).

Therefore, a possible mechanism to explain the closure of the North Makran is the interaction of a seamount chain and associated thickened oceanic crust with the margin of the Lut Block during the Late Cretaceous. This picture requires more data to be confirmed but seems more coherent with the evidence provided by this paper and by the recent literature.

6. Conclusion

In the available literature, the Bajgan Complex is regarded as a Paleozoic or older metamorphic basement (e.g., McCall, 1985; Hunziker et al., 2015), generally interpreted as the remnants of the small continental microplate whose collision with the Lut Block led to the closure of the North Makran oceanic basin (McCall, 1982; Omrani et al., 2017; Dorani et al., 2017; Burg, 2018; Sepidbar et al., 2020). Our study provides a completely different picture. Firstly, the Bajgan Complex includes meta-ophiolites consisting of MOR-type meta-gabbros and meta-basalts with the occurrence of OIB and E-MOR meta-basalts. The meta-ophiolites are associated to meta-sedimentary rocks, here interpreted as the sedimentary pelagic cover of the meta-ophiolites. U-Pb dating on zircons indicate that the magmatic ages of the meta-intrusive rocks range from 161 to 114 Ma, i.e., from Oxfordian to Aptian. These data obviously exclude a Paleozoic origin for the metamorphic rocks of the Bajgan Complex. In addition, the Bajgan Complex is affected by a polyphase deformation history that includes three deformation phases, namely D1, D2 and D3 phases. The P-T estimates indicate that the D1 phase was developed at conditions of blueschist metamorphic facies, whereas the D2 phase includes two different mineral assemblages. The early stage of the D2 phase occurs at P-T conditions corresponding to the boundary between blueschist and epidote amphibolite metamorphic facies, whereas the late stage of the D2 phase instead

occurs at greenschist metamorphic facies conditions. These structural and petrological data thus indicate that the deformation of the Bajgan Complex was acquired in a subduction setting by deep accretion and exhumation of the meta-ophiolites and related meta-sedimentary deposits within an accretionary wedge. A further important constraint is also provided by the age of the D2 phase that has been constrained to Cenomanian-Turonian (100-90 Ma) using Ar-Ar dating on white mica. The time constraint for the final exhumation of the Bajgan Complex is represented by middle Eocene non-metamorphic felsic dykes that intrude the Bajgan Complex when it was already exhumed at shallow crustal levels.

These results indicate that the Bajgan Complex represents a Cretaceous fossil accretionary wedge composed by a Late Jurassic-Early Cretaceous oceanic lithosphere rather than a continental basement of pre-Mesozoic age as previously thought. This conclusion opens a new scenario for the geodynamic reconstruction of the Makran region and it must be considered to understand the closure process of the North Makran oceanic basin.

Acknowledgments

The research has been funded by Darius Project (Head M. Marroni). This research benefits also by grants from PRA project of University of Pisa and from IGG-CNR, as well as from FIR-2017 and FIR-2018 Projects of the Ferrara University. R. Tassinari (University of Ferrara) is acknowledged for technical support with chemical analyses. Constructive and thorough reviews for the journal by A. Mohammadi and an anonymous reviewer have helped us improve the science and organization presented in the paper.

References

Agard, P., Plunder, A., Angiboust, S., Bonnet, G., Ruh, J., 2018. The subduction plate interface: rock record and mechanical coupling (from long to short timescales). Lithos 320, 537-566.

Agard, P., Yamato, P., Jolivet, L., Burov, E., 2009. Exhumation of oceanic blueschists and eclogites in subduction zones: timing and mechanisms. Earth-Science Reviews 92, 53-79.

Allègre, C. J., Minster, J.F., 1978. Quantitative models of trace element behavior in magmatic processes. Earth Planet. Sci. Lett. 38(1), 1-25.

Barbero, E., Delavari, M., Dolati, A., Saccani, E., Marroni, M., Catanzariti, R., Pandolfi, L., 2020a. The Ganj Complex reinterpreted as a Late Cretaceous volcanic arc: Implications for the geodynamic evolution of the North Makran domain (southeast Iran). J. Asian Earth Sci. https://doi.org/10.1016/j.jseaes.2020.104306.

Barbero, E., Delavari, M., Dolati, A., Vahedi, L., Langone, A., Marroni, M., Pandolfi, L., Zaccarini, F., Saccani, E., 2020b. Early Cretaceous Plume–Ridge Interaction Recorded in the Band-e-Zeyarat Ophiolite (North Makran, Iran): New Constraints from Petrological, Mineral Chemistry, and Geochronological Data. Minerals 10(12), 1100, https://doi.org/10.3390/min10121100

Barbero, E., Pandolfi, L., Delavari, M., Dolati, A., Saccani ,E., Catanzariti, R., Luciani, V., Chiari, M., ,Marroni, M., 2021. The western Durkan Complex (Makran Accretionary Prism, SE Iran): a Late

Cretaceous tectonically disrupted seamounts chain and its role in controlling deformation style. Geosci. Frontiers, 12, 101106.

Barbero, E., Zaccarini, F., Delavari, M., Dolati, A., Saccani, E., Marroni, M., Pandolfi, L., 2021b. New evidence for Late Cretaceous plume-related seamounts in the Middle East sector of the Neo-Tethys: Constraints from geochemistry, petrology, and mineral chemistry of the magmatic rocks from the western Durkan Complex (Makran Accretionary Prism, SE Iran. Lithos, 396–397, 106228. https://doi.org/10.1016/j.lithos.2021.106228

Barrier, E., Vrielynck, B., Brouillet, J.F., Brunet, M.F., 2018. Paleotectonic Reconstruction of the Central Tethyan Realm. Tectono-Sedimentary-Palinspastic maps from Late Permian to Pliocene. Atlas of 20 maps (scale: 1:15.000.000). CCGM/CGMW, Paris, http://www.ccgm.org.

Bayer, R., Chery, J., Tatar, M., Vernant, P., Abbassi, M., Masson, F., Nilforoushan, F., Doerflinger, E., Regard, V., Bellier, O., 2006, Active deformation in Zagros—Makran transition zone inferred from GPS measurements. Geoph. J. Int. 165(1), 373–381.

Beccaluva, L., Di Girolamo, P., Macciotta, G., Morra, V., 1983. Magma affinities and fractionation trends in ophiolites. Ofioliti 8 (3), 307-323

Bortolotti, V., Chiari, M., Kodra, A., Marcucci, M., Mustafa, F., Principi, G., and Saccani, E., 2004. New evidences for Triassic MORB magmatism in the northern Mirdita Zone ophiolites (Albania). Ofioliti 29, 247~~3~~-250~~46~~.

Bröcker, M., Omrani, H., Berndt, J., and Moslempour, M. E., 2021. Unravelling metamorphic ages of suture zone rocks from the Sabzevar and Makran areas (Iran): Robust age constraints for the larger Arabia–Eurasian collision zone. Journal of Metamorphic Geology, June 2020, jmg.12603. https://doi.org/10.1111/jmg.12603

Burg, J.-P., 2018. Geology of the onshore Makran accretionary wedge: Synthesis and tectonic interpretation. Earth Sci. Rev. 185, 1210-1231.

Burg, J.-P., Bernoulli, D., Smit, J., Dolati, A., Bahroudi, A., 2008. A giant catastrophic mud-and-debris flow in the Miocene Makran. Terra Nova 20, 188-193.

Burg, J.-P., Dolati, A., Bernoulli, D., Smit, J., 2013. Structural style of the Makran tertiary accretionary complex in SE Iran. In: Al Hosani, K., Roure, F., Ellison, R., Lokier, S. (Eds.), Lithosphere Dynamics and Sedimentary Basins: The Arabian Plate and Analogues. Frontiers in Earth Sciences, Springer, Heidelberg, pp. 239-259.

Cabanis, B., Leécolle, M., 1989. Le diagramme La/10-Y/15-Nb/8: un outil pour la discrimination des séries volcaniques et la mise en évidence des processus de mélange et/ou de contamination crustale. Compt. Rend. Acad. Sci.-Série 2 309(20), 2023-2029.

Chauvet, F., Lapierre, H., Maury, R. C., Bosch, D., Basile, C., Cotten, J., Brunet, P., Campillo, S., 2011. Triassic alkaline magmatism of the Hawasina Nappes: Post-breakup melting of the Oman lithospheric mantle modified by the Permian Neotethyan Plume. Lithos 122, 122–136.

Chiari, M., Bortolotti, V., Marcucci, M., Photiades, A., Principi, G., and Saccani, E., 2012. Radiolarian biostratigraphy and geochemistry of the Koziakas massif ophiolites (Greece). Bull. Soc. Géol. France 183(4), 287-306.

Cloos, M., Shreve, R. L., 1988. Subduction-channel model of prism accretion, melange formation, sediment subduction, and subduction erosion at convergent plate margins: 1. Background and description. Pure Appl. Geoph. 128(3), 455-500.

Delavari, M., Dolati, A., Marroni, M., Pandolfi, L., Saccani E., 2016. Association of MORB and SSZ ophiolites along the shear zone between Coloured Mélange and Bajgan Complexes (North Maran, Iran): Evidence from the Sorkhband area. Ofioliti, 41, 21-34.

Desmons, J., Beccaluva, L., 1983. Mid-Ocean ridge and island-arc affinities in ophiolites from Iran: Palaeographic implications. Chem. Geol. 39, 39-63.

Dilek, Y., Furnes, H., 2011. Ophiolite genesis and global tectonics: geochemical and tectonic fingerprinting of ancient oceanic lithosphere. Geol. Soc. Am. Bull. 123, 387-411.

Dolati, A., Burg, J.-P., 2013. Preliminary fault analysis and paleostress evolution in the Makran Fold-and-Thrust Belt in Iran. In: Al Hosani, K., Roure, F., Ellison, R., Lokier, S. (Eds.), Lithosphere Dynamics and Sedimentary Basins: The Arabian Plate and Analogues. Frontiers in Earth Sciences, Springer, Heidelberg, pp. 261–277.

Dorani, M., Arvin, M., Oberhänsli, R., Dargahi, S., 2017. P-T evolution of metapelites from the Bajgan complex in the Makran accretionary prism, south eastern Iran. Geochem. 77, 459–475.

Dubacq, B., Vidal, O., De Andrade, V., 2010. Dehydration of dioctahedral aluminous phyllosilicates: thermodynamic modelling and implications for thermobarometric estimates. Contrib. Mineral. Petrol. 159(2), 159.

Eftekhar-Nezhad, J., Arshadi, S., Mahdavi, M.A., Morgan, K.H., McCall, G.J.H., Huber, H., 1979. Fannuj Quadrangle Map 1:250000. Ministry of Mines and Metal, Geological Survey of Iran, Tehran.

Fagereng, Å., Cooper, A. F., 2010. The metamorphic history of rocks buried, accreted and exhumed in an accretionary prism: an example from the Otago Schist, New Zealand. Journal of Metam. Geol. 28(9), 935-954.

Ferrill, D.A., Morris, A.P., Evans, M.A., Burkhard, M., Groshong, R.H., Onasch, C.M., 2004. Calcite twin morphology: A low-temperature deformation geothermometer. J. Struct. Geol. 26, 1521–1529.

Frassi, C., Rebay, G., Marroni, M., Sayit, K., Göncüoğlu, M.C., Ellero, A., Ottria, G., Pandolfi L., 2020. Metamorphic imprint of ridge subduction on the Neo-Tethyan ophiolites from the Saka Unit (Central Pontides, Northern Turkey). J. Asian Earth Sci. 200, 104468.

Gansser, A., 1959. Ausseralpine ophiolith probleme. Eclogae Geol. Helv. 59: 831-848.

Ghazi, A.M., Hassanipak, A.A., Mahoney, J.J., Duncon, R.A., 2004. Geochemical characteristics, 40Ar-39Ar ages and original tectonic setting of the Band-e-Zeyarat/Dar Anar ophiolite, Makran accretionary Prism, S.E. Iran. Tectonophysics 193, 175-196.

Ghose, N.C., Chatterjee, N., Mukherjee, D., Kent, R.W. and Saunders, A.D., 2008. Mineralogy and geochemistry of the Bengal anorthosite massif in the Chotanagpur gneissic complex at the Eastern Indian Shield margin. Jour. Geol. Soc. India 72, 263-277.;

Glennie, K.W., Hughes Clarke, M.W., Boeuf, M.G.A., Pilaar, W.F.H., Reinhardt, B.M., 1990. Inter-relationship of Makran-Oman Mountains belts of convergence. In: Robertson, A.H.F., Searle, M.P., Ries, A.C. (Eds.), The Geology and Tectonics of the Oman Region. Geological Society, London Special Publications, pp. 773–786.

Guillot, S., Hattori, K., Agard, P., Schwartz, S., Vidal, O., 2009. Exhumation processes in oceanic and continental subduction contexts: a review. Subduction zone geodynamics, 175-205.

Haberland, C., Mokhtari, M., Babaei, H. A., Ryberg, T., Masoodi, M., Partabian, A., Lauterjung, J., 2021. Anatomy of a crustal-scale accretionary complex: Insights from deep seismic sounding of the onshore western Makran subduction zone, Iran. Geology 49(1), 3-7.

Hodges, K.V., 1991. Pressure–temperature–time paths. Ann. Rev. Earth Planet. Sci. 19, 207–236.

Hunziker, D., Burg, J.-P., Bouilhol, P., von Quadt, A., 2015. Jurassic rifting at the Eurasian Tethys margin: Geochemical and geochronological constraints from granitoids of North Makran, southeastern Iran. Tectonics 34, 571-593.

Kusky, T.M., Windley, B.F., Safonova, I., Wakita, K., Wakabayashi, J., Polat, A., Santosh, M., 2013. Recognition of ocean plate stratigraphy in accretionary orogens through Earth history: A record of 3.8billion years of sea floor spreading, subduction, and accretion. Gond. Res. 24, 501–547.

Lapierre, H., Samper, A., Bosch, D., Maury, R.C., Béchennec, F., Cotten, J., Demant, A., Brunet, P., Keller, F., Marcoux, J., 2004. The Tethyan plume: geochemical diversity of Middle Permian basalts from the Oman rifted margin. Lithos 74, 167–198.

Law, R.D., 2014. Deformation thermometry based on quartz c-axis fabrics and recrystallization microstructures: A review. J. Struct. Geol. 66, 129-161.

Marroni, M., Meneghini, F., Pandolfi, L., 2004. From accretion to exhumation in a fossil accretionary wedge: a case history from Gottero Unit (Northern Apennines, Italy). Geod. Acta 17(1), 41-53.

McCall, G.J.H., 1983. Mélanges of the Makran, southeastern Iran. In: In: McCall, G.J.H. (Ed.), Ophiolitic and related mélanges, Benchmark Papers in Geology 66. Hutchinson Ross Publishing Company, Stroudsburg, Pennsylvania, pp. 292–299.

McCall, G.J.H., 1985. Explanatory text of the Minab Quadrangle Map; 1:250,000; No. J13. Geological Survey of Iran, Tehran, pp. 530.

McCall, G.J.H., 1997. The geotectonic history of the Makran and adjacent areas of southern Iran. J. Asian Earth Sci. 15, 517-531

McCall, G.J.H., 2002. A summary of the geology of the Iranian Makran. In: Clift, P.D., Kroon, F.D., Gaedecke, C., Craig, J. (Eds.), The Tectonic and Climatic Evolution of the Arabian Sea Region, Geological Society of London Special Publications vol. 195, pp. 147-204.

McCall, G.J.H., Kidd, R.G.W., 1982. The Makran southeastern Iran: the anatomy of a convergent margin active from Cretaceous to present. In: Leggett, J.K. (Ed.), Trench-forearc geology: sedimentation and tectonics of modern and ancient plate margins, Geological Society of London Special Publications vol. 10, pp. 387-397.

Meneghini, F., Marroni, M., Moore, J.C., Pandolfi, L., Rowe, C.D., 2009. The processes of underthrusting and underplating in the geologic record: structural diversity between the Franciscan Complex (California), the Kodiak Complex (Alaska) and the Internal Ligurian Units (Italy). Geol. J. 44 (2), 126-152.

Meneghini, F., Pandolfi, L., Marroni, M., 2020. Recycling of heterogeneous material in the subduction factory: evidence from the sedimentary mélange of the Internal Ligurian Units, Italy. J. Geol. Soc. 177(3), 587-599.

Mohammadi, A., Burg, J.-P., Winkler, W., Ruh, J., von Quadt, A., 2016. Detrital zircon and provenance analysis of Late Cretaceous–Miocene onshore Iranian Makran strata: Implications for the tectonic setting. Geological Society of America Bulletin 128, 1481–1499. https://doi.org/10.1130/B31361.1

Mohammadi, A., Burg, J.-P., Guillong, M., von Quadt, A., 2017. Arc magmatism witnessed by detrital zircon U-Pb geochronology, Hf isotopes and provenance analysis of Late Cretaceous-Miocene sandstones of onshore western Makran (SE Iran). American Journal of Science, 317(8), 941–964. https://doi.org/10.2475/08.2017.03

Monsef, I., Rahgoshay, M., Pirouz, M., Chiaradia, M., Grégoire, M., and Ceuleneer, G., 2019. The Eastern Makran Ophiolite (SE Iran): evidence for a Late Cretaceous fore-arc oceanic crust. Int. Geol. Rev. 61 (11), 1313–1339.

Moslempour, M.E., Khalatbari-Jafari, M., Ghaderi, M., Yousefi, H., Shahdadi, S., 2015. Petrology, geochemistry and tectonics of the extrusive sequence of Fannuj-Maskutan Ophiolite, southeastern Iran. J. Geol. Soc. India 85, 604–618.

Mukherjee, D., Ghose, N. C., and Chatterjee, N., 2005. Crystallization history of a massif anorthosite in the eastern Indian shield margin based on borehole lithology. J. Asian Earth Sci. 25(1), 77-94.

O'Brien, T. M., Grove, M., 2020. Subduction accretion, thermal overprinting, and exhumation of high-pressure/low-temperature metasedimentary rocks of the south-central Brooks range. Int. Geol. Rev. https://doi.org/10.1080/00206814.2020.1841684.

Okamato, K., Maruyama, S., 1999. High-pressure sythesis of lawsonite in the MORB + H2O system. Am. Miner. 84, 362–373.

Omrani, H., Moazzen, M., Oberhänsli, R. and Moslempour, M.E., 2017. Iranshahr blueschist: subduction of the inner Makran oceanic crust. J. Met. Geol. 35(4), 373-392.

Passchier, C.W., Trouw, R.A.J., 2005. Microtectonics. Berlin, New York, Springer 16, 366 pp.

Peacock, S.M., 1996. Thermal and petrologic structure of subduction zones. In: Bebout, G.E., et al. (Eds.), Subduction: Top to Bottom. Am. Geophys. Union, Geophys. Monograph 96, 119-133.

Pearce, J.A., 2008. Geochemical fingerprinting of oceanic basalts with applications to ophiolite classification and the search for Archean oceanic crust. Lithos 100, 14–48.

Platt, J.P., 1986. Dynamics of orogenic wedges and the uplift of high-pressure metamorphic rocks. Geol. Soc. Am. Bull. 97(9), 1037-1053.

Platt, J.P., Leggett, J.K., Young, J., Raza, H., Alam, S., 1985. Large-scale sediment underplating in the Makran accretionary prism, southwest Pakistan. Geology 13 (7), 507–511

Platt, J.P., Xia, H. and Schmidt, W.L., 2018. Rheology and stress in subduction zones around the aseismic/seismic transition. Progr. Earth Plan. Sci., 5(1), 1-12.

Plunder, A., Agard, P., Chopin, C., Pourteau, A., Okay, A.I., 2015. Accretion, underplating and exhumation along a subduction interface: From subduction initiation to continental subduction (Tavşanlı zone, W. Turkey). Lithos 226, 233-254.

Ramsay, J.G. 1967. Folding and fracturing of rocks. New York: McGraw-Hill.

Ruh, J.B., 2020. Numerical modeling of tectonic underplating in accretionary wedge systems. Geosphere 16(6), 1385-1407.

Saccani, E., 2015. A new method of discriminating different types of post-Archean ophiolitic basalts and their tectonic significance using Th-Nb and Ce-Dy-Yb systematics. Geosci. Frontiers 6, 481-501.

Saccani, E., Allahyari, K., and Rahimzadeh, B., 2014. Petrology and geochemistry of mafic magmatic rocks from the Sarve-Abad ophiolites (Kurdistan region, Iran): Evidence for interaction between MORB-type asthenosphere and OIB-type components in the southern Neo-Tethys Ocean. Tectonophysics 621, 132-147.

Saccani, E., Allahyari, K., Beccaluva, L., Bianchini, G., 2013. Geochemistry and petrology of the Kermanshah ophiolites (Iran): Implication for the interaction between passive rifting, oceanic

accretion, and OIB-type components in the Southern Neo-Tethys Ocean. Gond. Res. 24, 392–411.

Saccani, E., Delavari, M., Dolati, A., Marroni, M., Pandolfi, L., Chiari, M., Barbero E., 2018. New insights into the geodynamics of Neo-Tethys in the Makran area: Evidence from age and petrology of ophiolites from the Coloured Mélange Complex (SE Iran). Gond. Res. 62, 306-327.

Saccani, E., Dilek, Y., Marroni, M., Pandolfi, L., 2015. Continental margin ophiolites of Neotethys: Remnants of Ancient Ocean–Continent Transition Zone (OCTZ) lithosphere and their geochemistry, mantle sources and melt evolution patterns. Episodes 38, 230–249.

Saccani, E., Photiades, A., and Padoa, E., 2003. Geochemistry, petrogenesis and tectono-magmatic significance of volcanic and subvolcanic rocks from the Koziakas Mélange (Western Thessaly, Greece). Ofioliti 28, 43-57.

Samimi Namin, M., 1982. Geological Map of Taherui 1:250000 Scale. Tehran: Ministry of Mines and Metal, Geological Survey of Iran.

Samimi Namin, M., 1983. Geological Map of Minab 1:250000 Scale. Tehran: Ministry of Mines and Metal, Geological Survey of Iran.

Schmidt, M.W., 1992. Amphibole composition in tonalite as a function of pressure: an experimental calibration of the Al-in-hornblende barometer. Contrib. Mineral. Petrol 110, 304-310.

Schmidt, W. L., Platt, J. P., 2018. Subduction, accretion, and exhumation of coherent Franciscan blueschist-facies rocks, northern Coast Ranges, California. Lithosphere 10(2), 301-326.

Schoene, B., 2014. 4.10-U–Th–Pb Geochronology. Treatise on geochemistry, 4, 341-378.

Scholl, D. W., and von Huene, R., 2007. Crustal recycling at modern subduction zones applied to the past—Issues of growth and preservation of continental basement crust, mantle geochemistry, and supercontinent reconstruction. Geol. Soc. Am. Mem. 200, 9-32.

Sepidbar, F., Lucci, F., Biabangard, H., Zaki Khedr, M., Jiantang, P., 2020. Geochemistry and tectonic significance of the Fannuj-Maskutan SSZ-type ophiolite (Inner Makran, SE Iran). International Geology Review https://doi.org/10.1080/00206814.2020.1753118

Shellnutt, J. G., Dostal, J., Keppie, J. D., Keppie, D. F., Roeske, S.M., 2020. Formation of Anorthositic Rocks within the Blair River Inlier of Northern Cape Breton Island, Nova Scotia (Canada). Lithosphere 2020 (1): 8825465. doi: https://doi.org/10.2113/2020/8825465

Sun, S.S., McDonough, W.F., 1989. Chemical and isotopic systematics of oceanic basalts: implications for mantle composition and processes. In: Saunders, A.D., Norry, M.J. (Eds.), Magmatism in the Ocean Basins, Geological Society of London Special Publication vol. 42, pp. 313-345.

Syracuse, E.M., van Keken, P.E., Abers, G. A., 2010. The global range of subduction zone thermal models. Phys. Earth Plan. Inter. 183, 73-90.

Tullis, J., 2002. Deformation of granitic rocks: experimental studies and natural examples. Rev. Mineral. Geochem. 51(1), 51-95.

Vidal, O., Parra, T., 2000. Exhumation paths of high-pressure metapelites obtained from local equilibria for chloriteorite-phengite assemblage. Geol. J. 35, 139-161.

Vidal, O., De Andrade, V., Lewin, E., Munoz, M., Parra, T., Pascarelli, S. 2006. P–T-deformation-Fe2+/Fe3+mapping at the thin section scale and comparison with XANES mapping: application to a garnet-bearing metapelite from the Sambagawa metamorphic belt (Japan). J. Metam. Geol. 24, 669-683.

von Huene, R., Scholl, D.W., 1991, Observations at convergent margins concerning sediment subduction, subduction erosion, and the growth of continental crust. Rev. Geophys. 29, 279–316.

Whitney, D. L., Evans, B. W., 2010. Abbreviations for names of rock-forming minerals. Am. Min. 95, 185-187.

Winchester, J.A., Floyd, P.A., 1977. Geochemical discrimination of different magma series and their differentiation products using immobile elements. Chem. Geol. 20, 325–343.

Wood, D. A., 1980. The application of a Th-Hf-Ta diagram to problems of tectonomagmatic classification and to establishing the nature of crustal contamination of basaltic lavas of the British Tertiary Volcanic Province. Earth Planet. Sci. Lett. 50(1), 11-30.

CAPTIONS

Figure 1-Regional map depicting topography and tectonic features of Iran. In the rectangle a close-up on the tectonic setting of Makran area is inserted. The rectangle enclose Figures 2.

Figure 2-Simplified geological-structural map of the North Makran Domain showing the different tectonic units (Eftekhar-Nezhad et al., 1979; Samimi Namin, 1982, 1983; Burg, 2018; Barbero et al., 2020b). The red box indicates the area shown in Figure 3.

Figure 3-Simplified geological map of the Bajgan Complex (modified from Samimi Namin, 1982 and modified according to our original fieldwork and photointerpretation with satellite images) and related geological cross-section.

Figure 4-Field occurrence of the main lithotypes recognized in the Bajgan Complex. (a) meta-serpentinites body in the Deh Kahan area; (b) Layered meta-gabbros east of Deh Kahan Village.; (c) small stock of meta-plagiogranites (mp) associated with meta-gabbros (mg) in the Kuh-e-Govajag area; (d) garnet-bearing metavolcanics. The bands show different amphiboles composition; (e) meta-volcanoclastites (mv) associated with quarzites (mq); (f) The fine- to medium-grained impure marbles (m) alternated with micaschists (ms) in the Faryab Mine area.

Figure 5-Nb/Y vs. Zr/Ti discrimination diagram of Winchester and Floyd (1977) modified by Pearce (1996) for meta-ophiolitic rocks from the Bajgan Complex.

Figure 6-N-MORB normalized incompatible element patterns for meta-ophiolitic rocks from the Bajgan Complex. The compositions of modern enriched-type (E-) mid-ocean ridge basalts (MORB) and alkaline ocean island basalt (OIB), as well as normalizing values are from Sun and McDonough (1989).

Figure 7-a) Th-Ta-Hf/3 (Wood, 1980), (b) La/10-Nb/8-Y/15 (Cabanis and Lécolle, 1989), and N-MORB-normalized Th-Nb (Saccani, 2015) discrimination diagrams, and d) Zr/Y vs. Zr/Nb diagram for meta-ophiolitic rocks from the Bajgan Complex. Abbreviations, MORB: mid-ocean ridge basalt, N-: normal type, E-: enriched type, P-: plume type, D-: depleted type, MTB: medium-Ti basalts, IAT: island arc tholeiite, CAB: calc-alkaline basalt; OIB: alkaline oceanic within-plate basalt, SSZ-CE: supra-subduction zone component enrichment trend, OIB-CE: OIB (plume-type) component enrichment trend, FC: fractional crystallization trend. The compositional variation of different types of volcanic rocks and dykes are also shown for comparison in c) and d). Data for compositional fields in c) are from Saccani (2015). Fields in d) show the compositional variation for different types of basalts from the Zagros belt ophiolites (Saccani et al., 2013, 2014); Oman ophiolites (Chauvet et al., 2011; Lapierre et al., 2004), and Eastern Mediterranean ophiolites (Saccani et al., 2003; Bortolotti et al., 2004; Chiari et al., 2012). The dashed line in d) represents the mixing line between OIB and N-MORB. Normalization values, as well as the composition of typical modern N-MORB, EMORB, and OIB (stars) are from Sun and McDonough (1989).

Figure 8-Mesoscopic features of D1, D2 and D3 deformation phase recognized in the Bajgan Complex. (a) Meta-volcanoclastites showing type 3 fold interference pattern (Ramsay, 1967) between F2 and F3 folds. The axial planes of D3 (AP3) and D2 (AP2) phases are indicated as well as the S1 schistosity. A possible hinge of D1 phase is indicated by the white arrow; (b) well

developed D2 phase fold (F2) in the meta-volcanoclastites. The main foliation S2 is indicated by the red line, the D1 phase schistosity (S1) is also indicated; (c) superposition between F2 and F3 folds in the marbles. The S1 and S2 schistosities are indicated. (d) well developed F3 fold in the calcschists. The D3 phase axial plane (AP3) and the D2 phase foliation (S2) are indicated.

Figure 9-Stereographic projections of the main structural elements documented in the field (equal area, lower hemisphere). The planar structural elements (i.e., S2 foliation, D2 shear zones, S3 foliation, D3 shear zones, and S4 foliation) are projected as pole to plane. The main S2 foliation is represented using 1% contour lines.

Figure 10-Microstructures of the Bajgan Complex. (a) Photomicrograph meta-gabbros. The S2 foliation (S2) is highlighted by pale blue elongated Amp crystals ± Quartz ± Feldspar ± Ep ± Opq (plane-polarized light). (b) Photomicrograph of meta-volcanic rocks showing F2 fold and S2 axial plane foliation (S2) overprinting F1 fold (plane-polarized light). S0: bedding; AP1: F1 fold axial plane. (c) Relics of S1 foliation (S1) marked by aggregates of Chlorite and Ph oriented orthogonal to the S2 foliation (S2). Red arrow: dragging structure in Quartz; yellow arrow: lobate grain boundaries in Quartz; dotted red line: straight grain boundaries in Quartz that meet in 120° triple points (cross-polarized light). (d) Photomicrograph of micaschist showing S2 foliation (S2) highlighted by irregular layers of Ph + Chlorite crystals wrapping Feldspar (Feld) crystal, locally showing thin deformation twins, and Quartz crystals with straight grain boundaries at 120° triple points (black arrow) and scarce lobate grain boundaries (plane polarized light). (e) Photomicrograph of D2 shear zones with S-C’ structures and s-type porphyroclasts of Feldspar pointing to a top-to-the S-SW. Sm: mylonitic foliation; C’: C’ shear plane; (plane polarized light). (f) S2 foliation (S2) in impure marble (Cal; cross-polarized light). (g) Photomicrograph of impure

marble with large Cal crystal showing thick and irregular deformation twins (Type IV of Ferrill et al., 2004) (white arrow; cross-polarized light).(h) Photomicrograph of S3 foliation (S3) in micaschist. S1: S1 foliation; S2: S2 foliation (plane-polarized light).

Figure 11-Compositional maps of sample MK706 and related P-T diagrams showing the results of Chlorite-Quartz-wt, Ph-Quartz-wt and Chlorite-Ph-Quartz-wt methods for (a) the D1 phase, (b) the D2-peak and (c) the late-D2 events. In the compositional maps (end-member content, %) the sampled areas are marked by white boxes. In the P-T diagrams, all blue components are referred to the Chlorite-Quartz-wt method, red components are related to the Ph-Quartz-wt method and black components are related to the Chlorite-Ph-Quartz-wt method. In blue: the data distributions (i.e. Chlorite) are represented by histograms that define the range of stabilities related to the three groups of Chlorite (blue areas). In red: each line represents the stability of a single Ph analyses at different conditions of water activity and red circles indicate the point in which the water activity is set to 0.8; red areas indicate the P ranges defined basing on the Ph-Quartz-wt method's results. In black: black crosses indicate the position of the equilibrium reached by each single Chlorite-Ph couple; smallest crosses indicate the best optimized result. An example of the reactions convergence (Chlorite-Ph-Quartz-wt method) are reported in the small black box within the P-T diagram (yellow circle is equivalent to black cross).

Figure 12-Altot in Ca-Amp as function of pressure. Dense dashed line represents calibration of Schmidt (1992). The error associated to this calibration is 0.05 GPa (grey area). Light blue lines represent single Amp analyzed in this study. Orange area (and related error in pale orange) represents the P range obtained with the match between the Amp analysis with the Schmidt's calibration.

Figure 13-$^{206}Pb/^{238}U$ age distribution of concordant and sub-concordant (discordance<±10%) data. The weighted average age and the relative Mean Square Weighted Deviates (MSWD) are also reported. Representative CL features of Zircon grains from MK701A, MK704 and MK705 samples. White bar is 20μm. Dotted circles refer to LA-ICP-MS spot locations.

Fig. 14-Results of $^{40}Ar–^{39}Ar$ laser step-heating experiments on White mica separates from sample Mk463, MK706 and MK707.). Plateau steps are red, rejected steps are blue.

Fig. 15-2D sketch (not to scale) of the subduction system at Late Cretaceous time, showing the tectono-metamorphic evolution of the Bajgan Complex. The zoom shows a schematic representation of the path made by the Bajgan Complex within the subduction channel at the plate interface between the basal and roof décollements. The possible locations of the D1, early D2, late D2 and D3 phases is also shown. The arrows indicate the pattern of flow in a subduction channel according to Platt et al. (2018). In the PT diagram, the three boxes represent three different stages of the metamorphic path reconstructed for the Bajgan Complex. Metamorphic facies boundaries from Okamato and Maruyama (1999).

Table 1-Major (wt.%) and trace (ppm) element analyses of meta-ophiolitic rocks from the Bajgan Complex. Abbreviations. XRF: X-ray fluorescence spectrometry; ICP-MS: inductively coupled plasma-mass spectrometry; n.d.: not detectable; b.d.l.: below detection limit; *: except when otherwise indicated. Mg# = 100 x Mg/(Mg+Fe). Fe2O3=0.15 x FeO. Normalizing values for REE ratios are from Sun and McDonough (1989).

Table 2-Results of zircon LA-ICP-MS U-Pb age determination of the samples MK 701A, 704 and 705A.

Table 3 – Results of chemical abrasion isotope-dilution thermal ionization mass spectrometry (CA-ID-TIMS) determination of the sample M328B.

Author Agreement Statement

We the undersigned declare that this manuscript is original, has not been published before and is not currently being considered for publication elsewhere.

We confirm that the manuscript has been read and approved by all named authors and that there are no other persons who satisfied the criteria for authorship but are not listed.

We further confirm that the order of authors listed in the manuscript has been approved by all of us. We understand that the Corresponding Author is the sole contact for the Editorial process.

He/she is responsible for communicating with the other authors about progress, submissions of revisions and final approval of proofs

Signed by all authors as follows: *Luca Pandolfi, Edoardo Barbero, Michele Marroni, Morteza Delavari, Asghar Dolati, Maria Di Rosa, Chiara Frassi, Antonio Langone, Federico Farina, Christopher S. MacDonald, Emilio Saccani*

CRediT author statement

Luca Pandolfi: Writing- Original draft preparation, Field investigations, Conceptualization

Edoardo Barbero: Writing- Original draft preparation, Field investigations, Conceptualization

Michele Marroni: Writing- Original draft preparation, Conceptualization, Funding acquisition

Morteza DelavarI: Field investigations, Data curation, Conceptualization,

Asghar Dolati: Field investigations, Data curation, Conceptualization

Maria Di Rosa: laboratory analyses, Data curation, Conceptualization

Chiara Frassi: Writing- Original draft preparation, laboratory analyses, Conceptualization

Antonio Langone: laboratory analyses, Data curation

Federico Farina: laboratory analyses, Data curation

Christopher S. MacDonald: laboratory analyses, data curation

Emilio Saccani: Conceptualization, Data curation, Funding acquisition

Declaration of interests

☒ The authors declare that they have no known competing financial interests or personal relationships that could have appeared to influence the work reported in this paper.

☐The authors declare the following financial interests/personal relationships which may be considered as potential competing interests:

Highlights

- The Bajgan Complex consists of meta-ophiolites
- The mafic rocks have MOR-, OIB- and E-MOR affinity
- The ages of intrusive protholiths range from Late Jurassic to Early Cretaceous
- The Bajgan Complex represents a Cretaceous fossil accretionary wedge

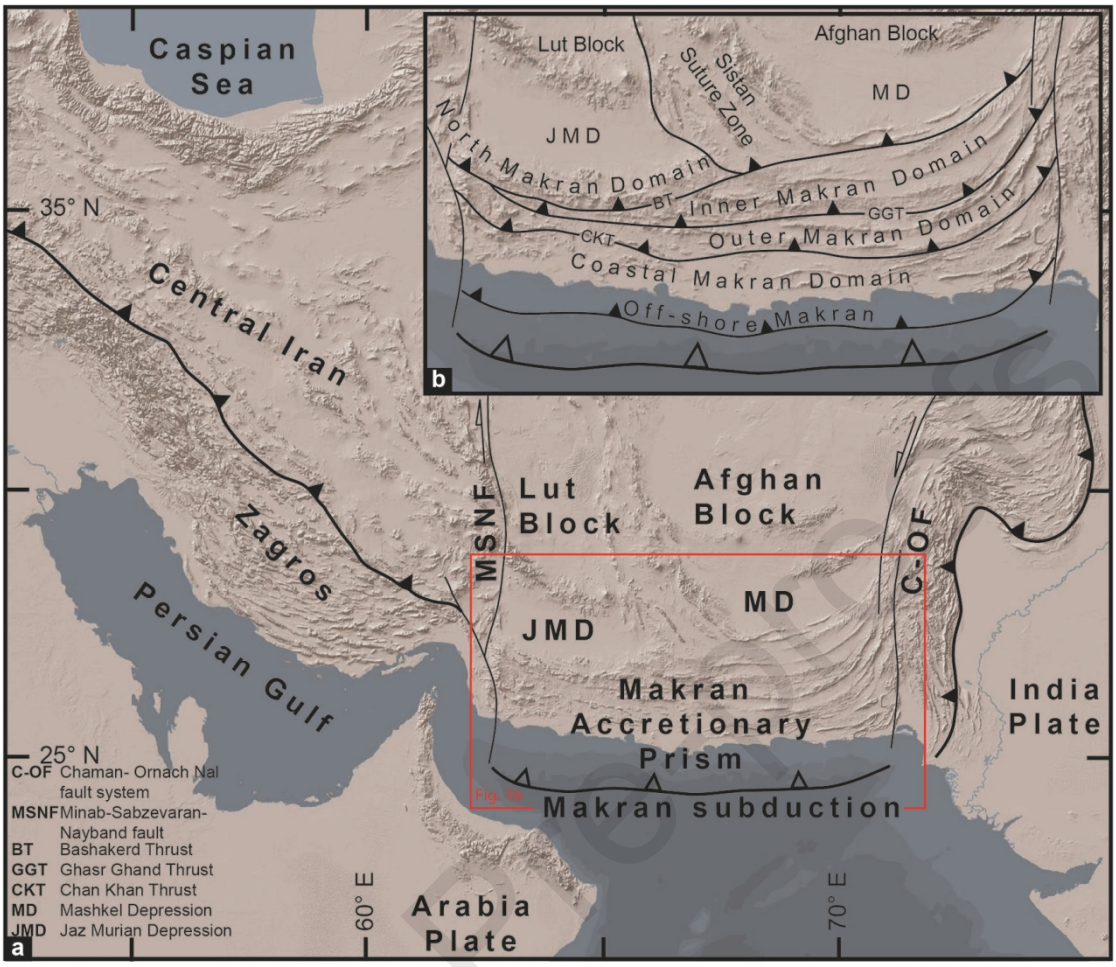

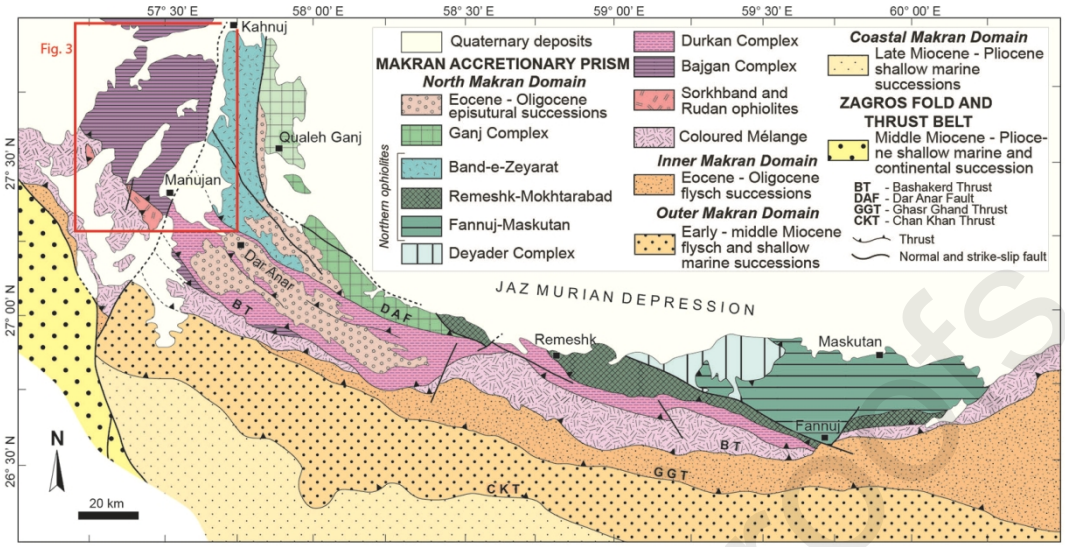

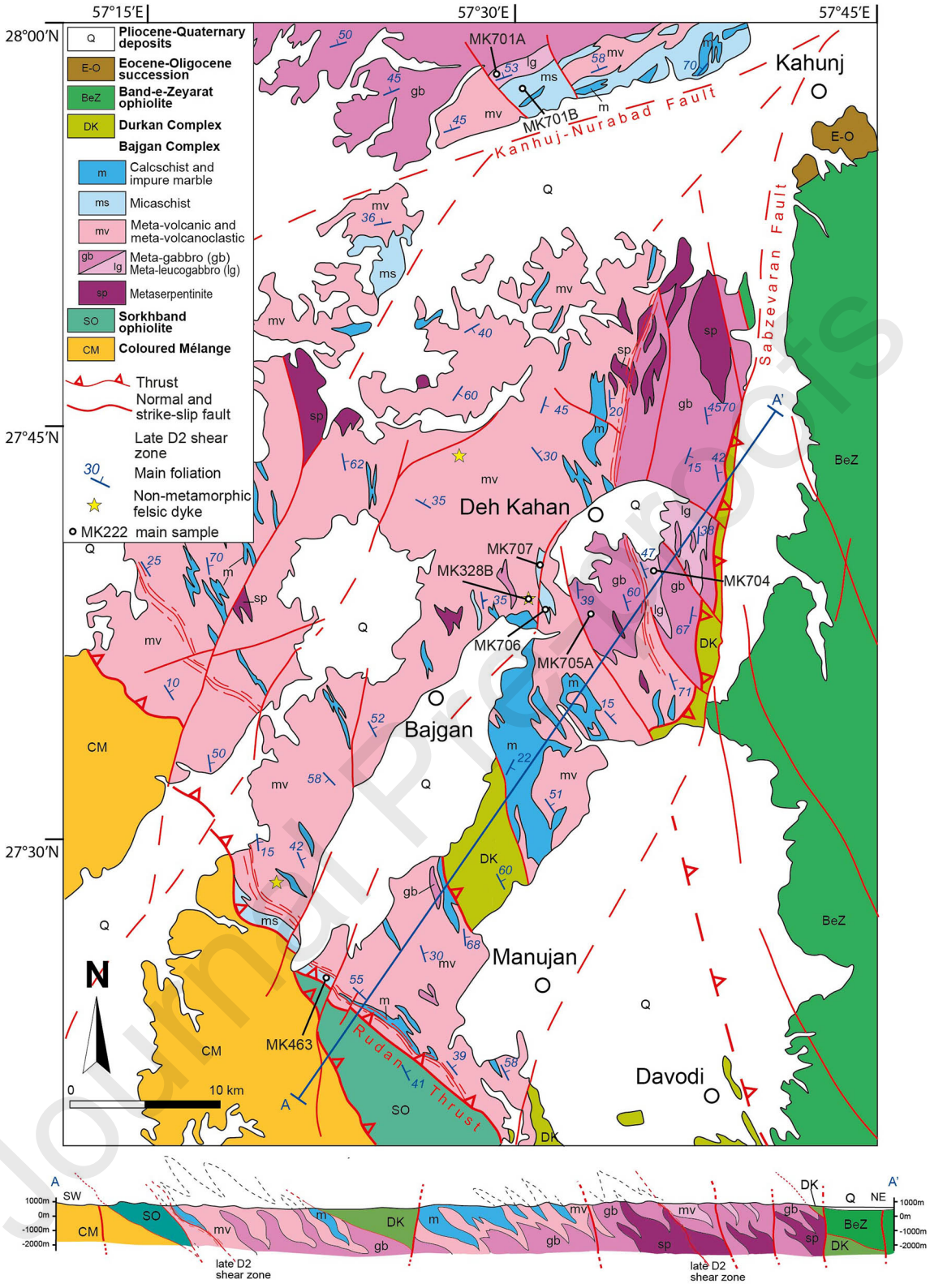

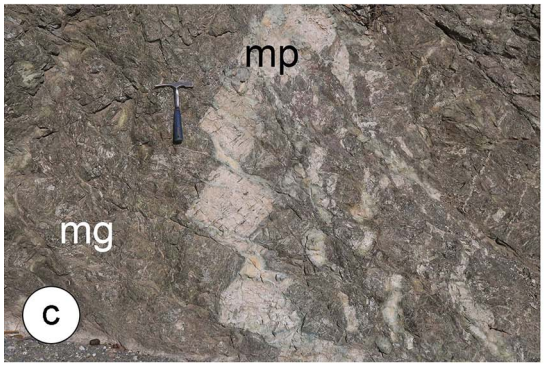

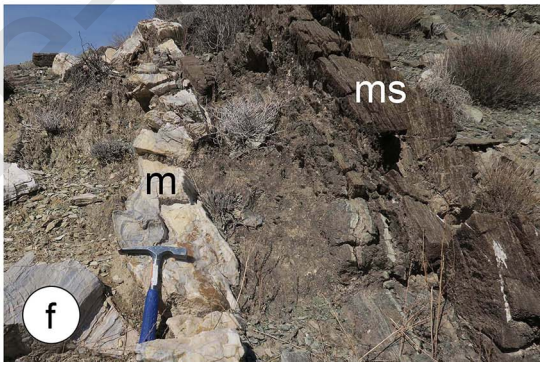

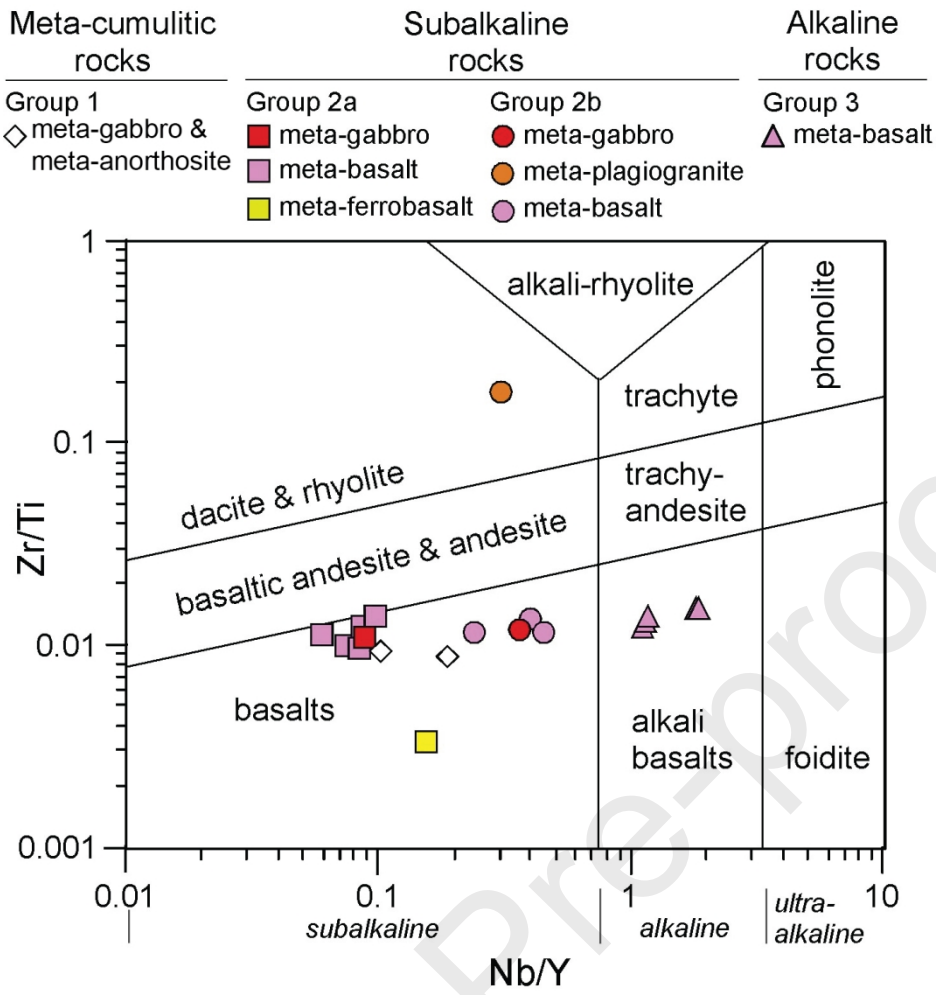

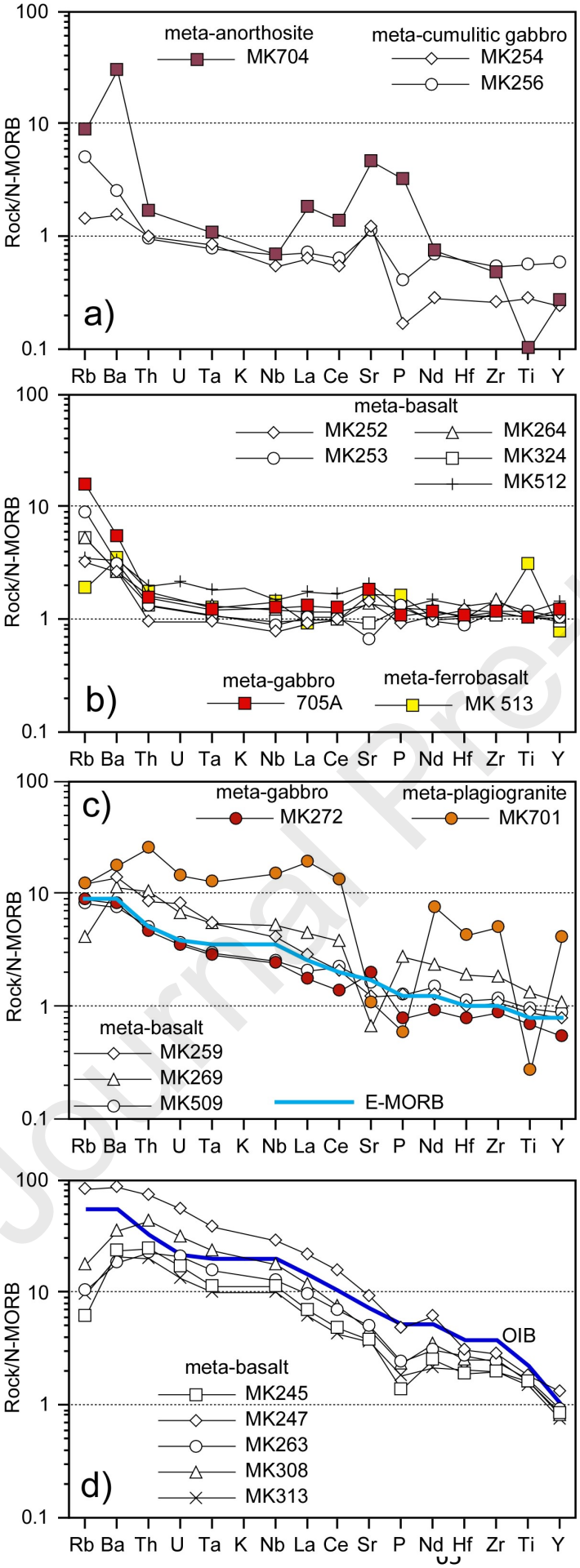

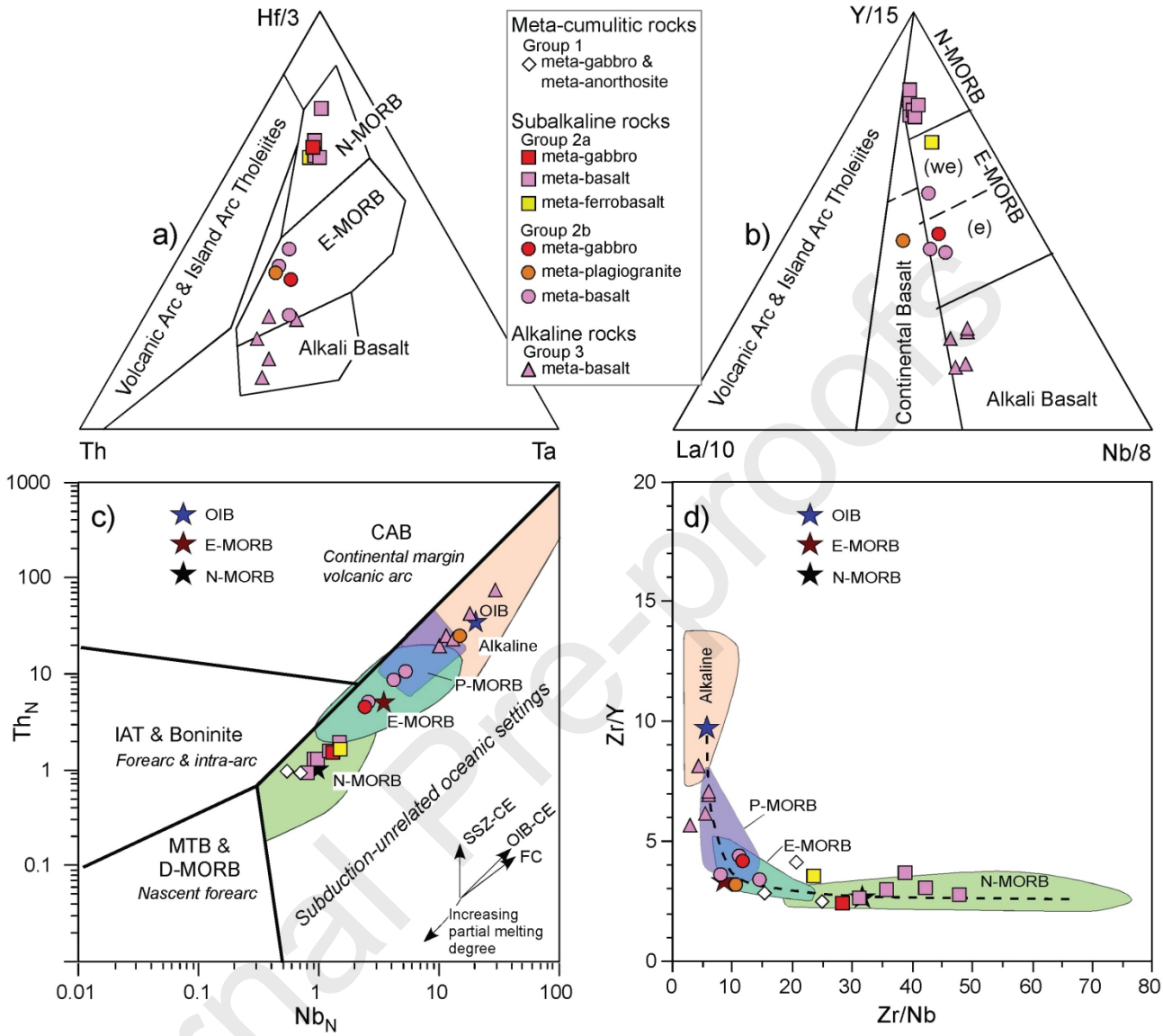

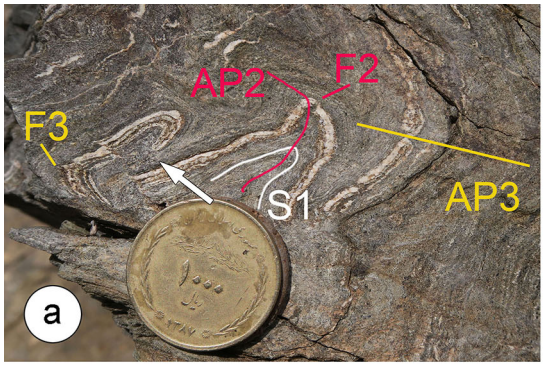
AP2
F2
F3
S1
AP3
a

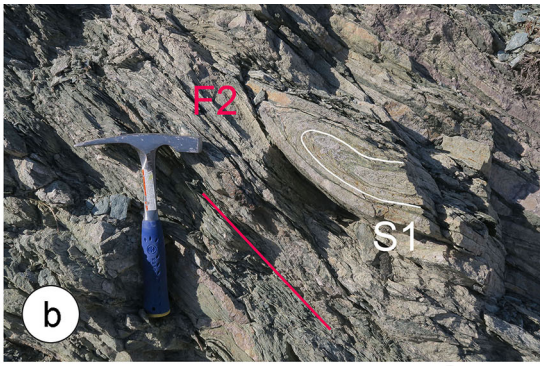
F2
S1
b

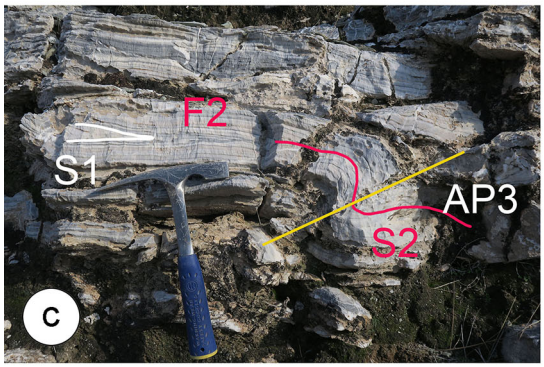
F2
S1
AP3
S2
c

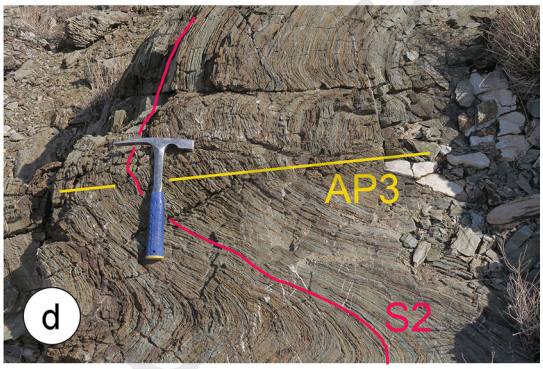
AP3
S2
d

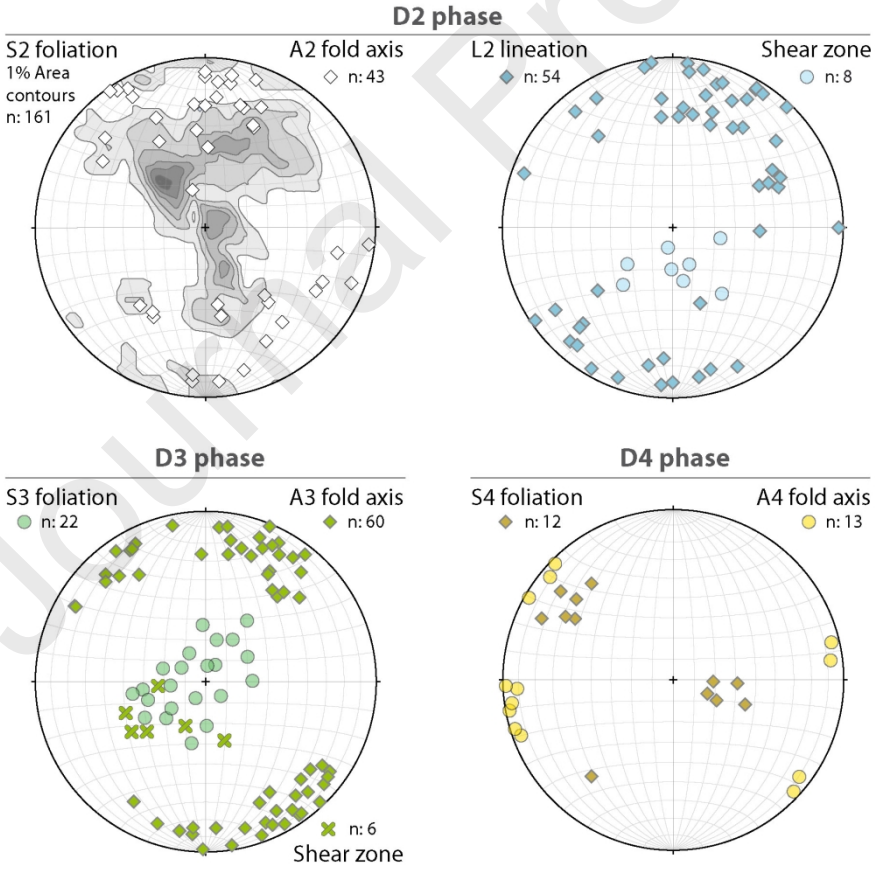
D2 phase
S2 foliation
1% Area
contours
n: 161
A2 fold axis
n: 43
L2 lineation
n: 54
Shear zone
n: 8
D3 phase
S3 foliation
n: 22
A3 fold axis
n: 60
n: 6
Shear zone
D4 phase
S4 foliation
n: 12
A4 fold axis
n: 13

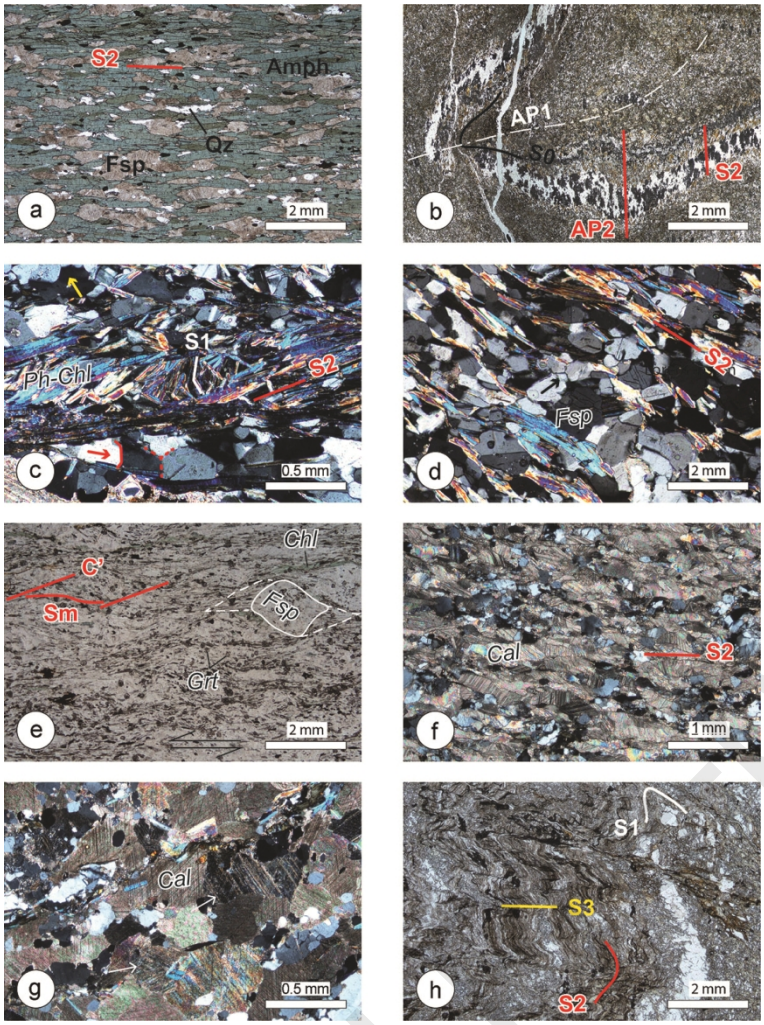

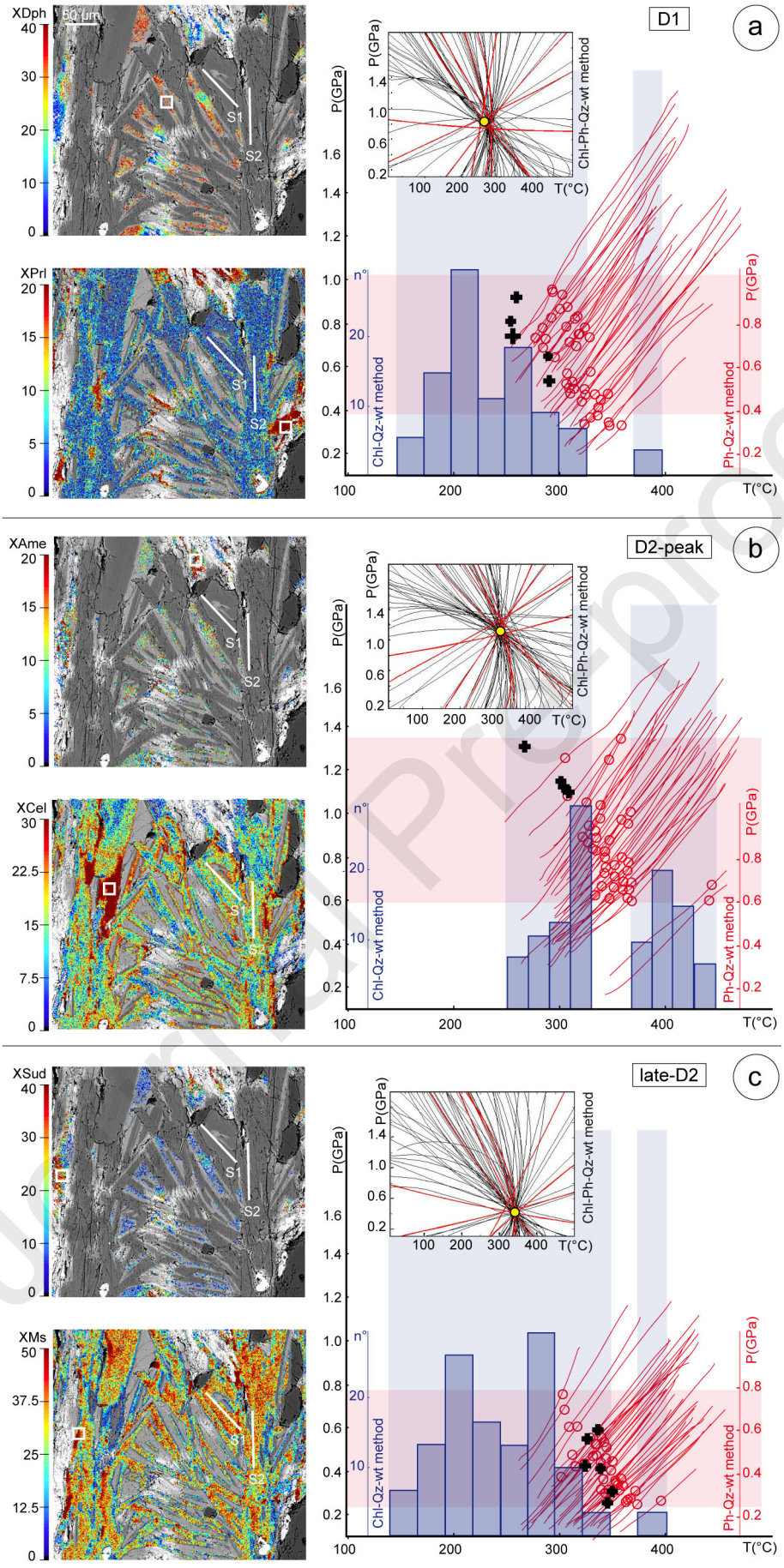

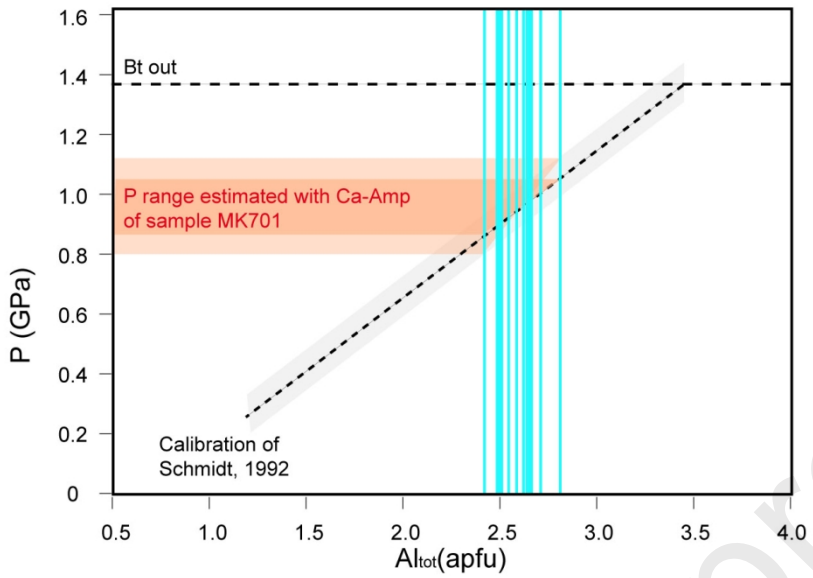

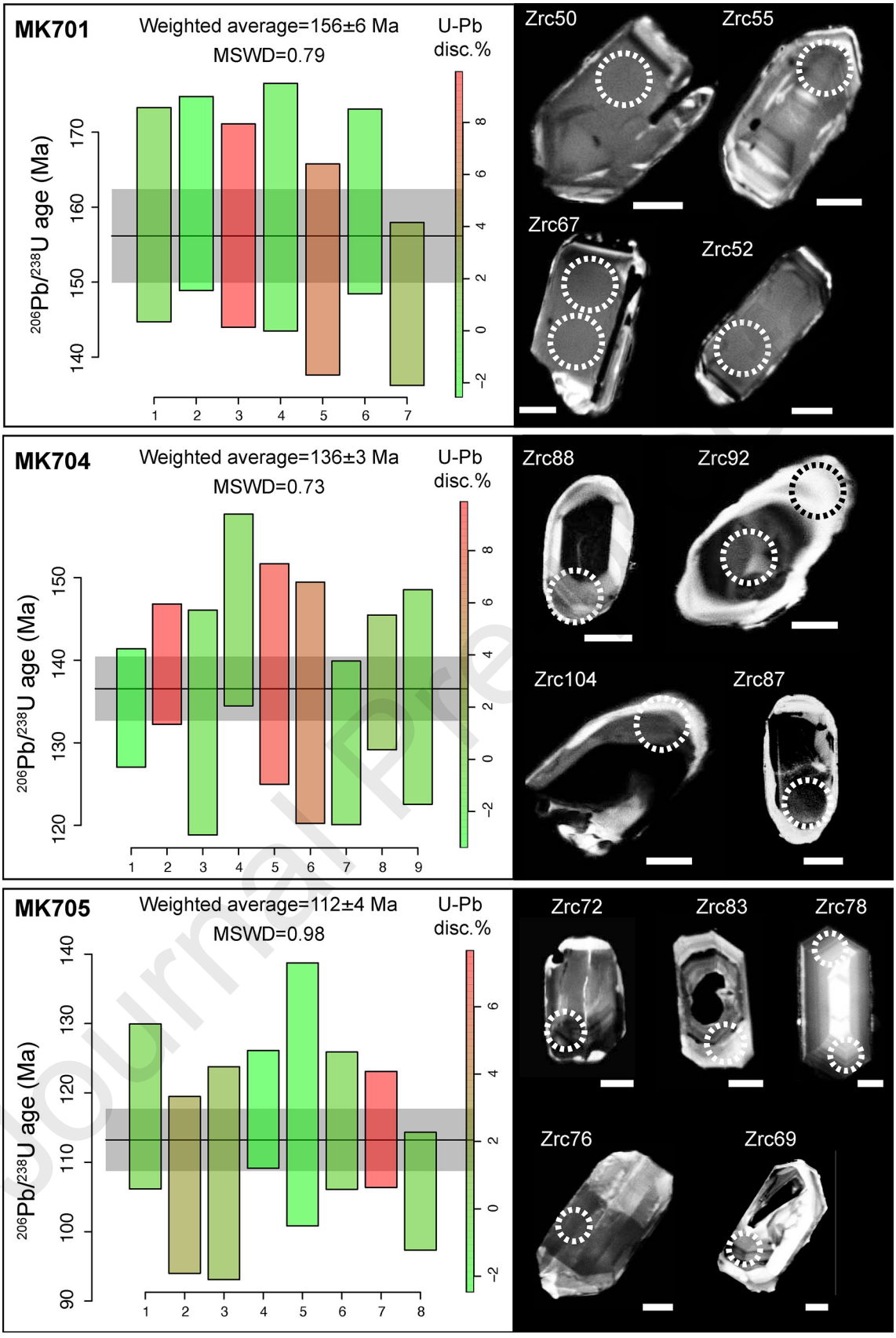

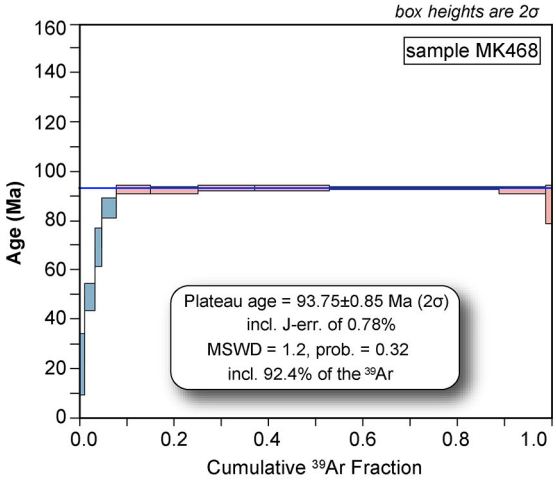

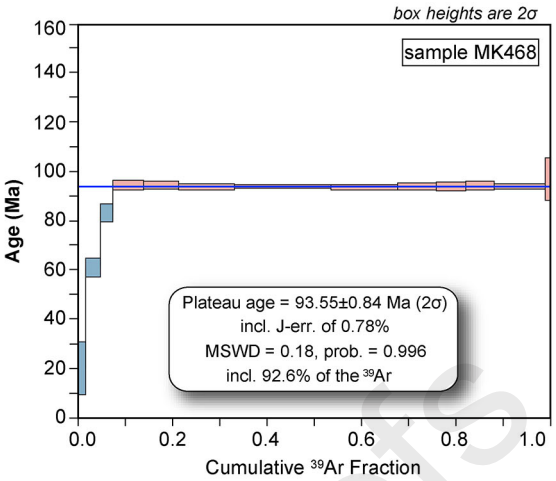

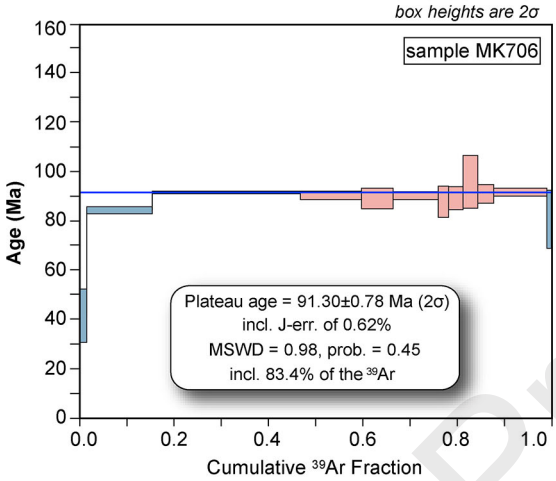

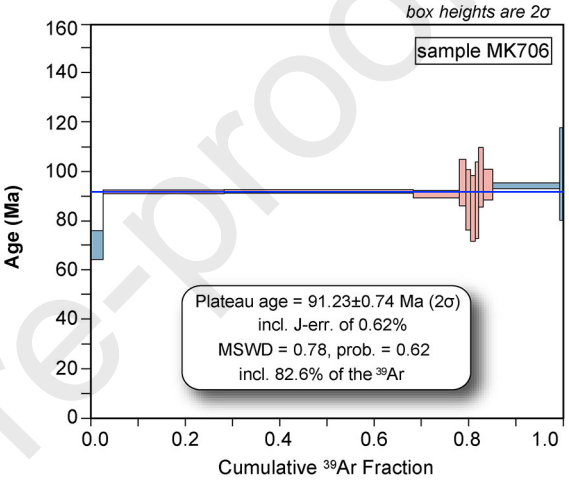

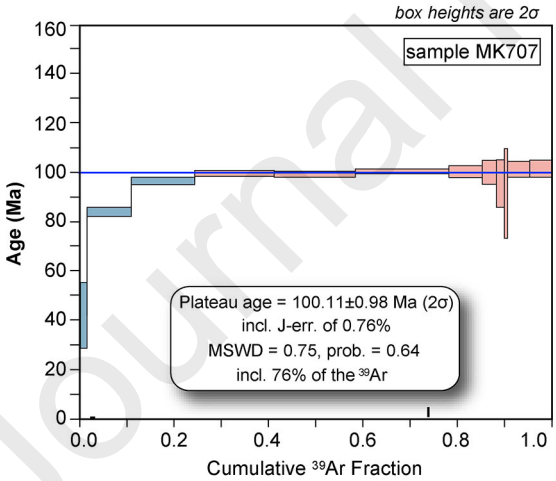

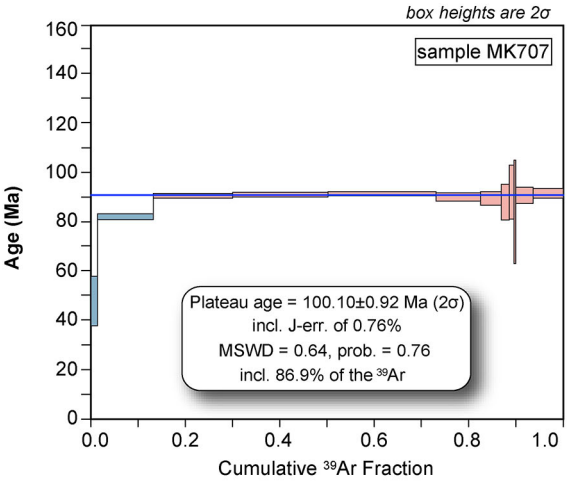

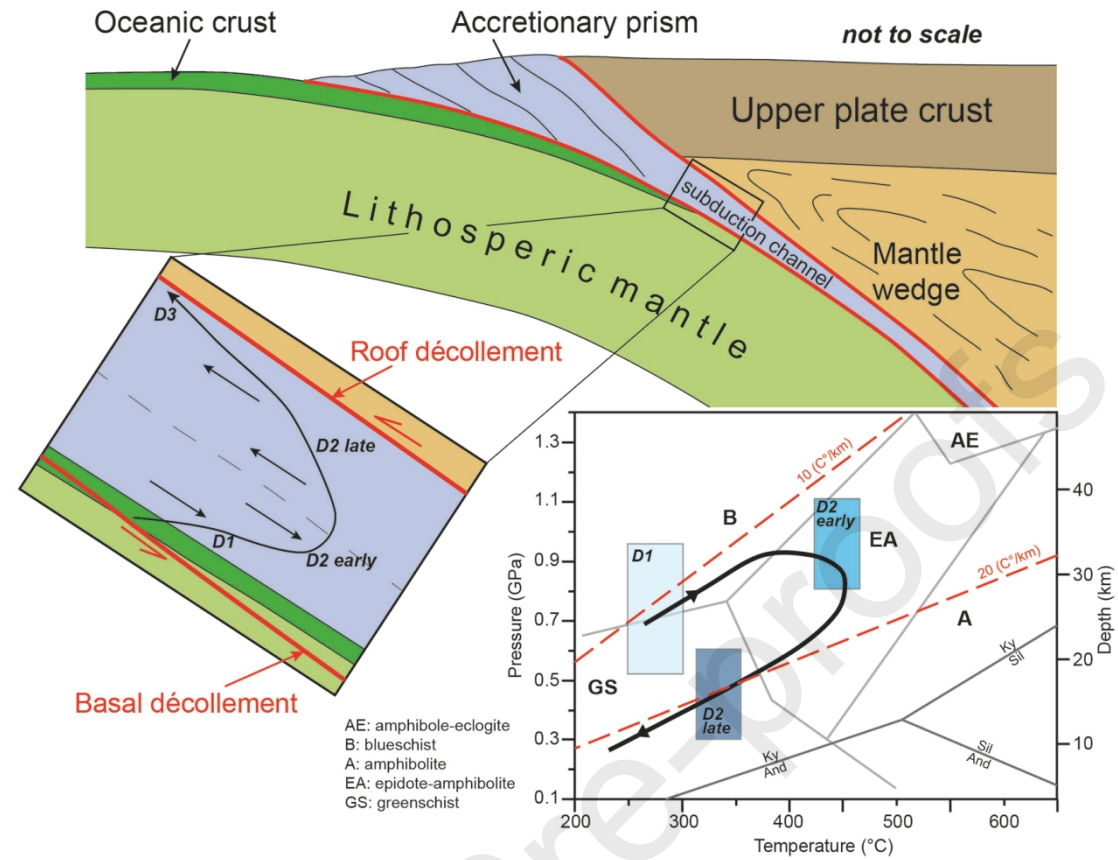

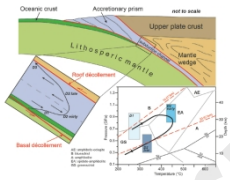

Supplementary Table 1

Unit	meta-mafic cumulitic rocks			Group 1 (N-MORB) meta-intrusive and meta-volcanic rocks							Group 2 (E-MORB) meta-intrusive and meta-volcanic rocks					Group 3 (Alkaline) meta-volcanic rocks						
Sample	MK704	MK254	MK256	MK705A	MK252	MK253	MK264	MK324	MK 512	MK 513	MK272	MK701	MK259	MK269	MK 509	MK245	MK247	MK263	MK308	MK313	Relative	Detection
Protholith	anorthosite	gabbro	gabbro	gabbro	bas	bas	bas	bas	bas	bas	gabbro	plag-gr	bas	bas	bas	bas	bas	bas	bas	bas	Error (%)	limits
Age	136,6 Ma			118,8 Ma								156,2 Ma										
(wt%)																						
SiO_2	60,16	48,21	49,83	50,01	49,09	50,25	48,35	49,00	47,79	42,48	50,56	71,19	50,51	50,30	49,57	42,82	46,50	42,62	47,98	48,98	0,5	0,05
TiO_2	0,12	0,35	0,71	0,67	1,28	1,43	1,29	1,35	1,44	3,85	0,88	0,35	1,12	2,72	1,21	1,96	2,33	2,07	2,02	1,84	0,9	0,01
Al_2O_3	17,31	15,53	14,61	14,92	13,43	14,72	14,29	13,81	14,18	12,25	14,99	12,59	14,42	13,69	13,40	13,48	15,60	13,81	12,99	14,09	2,5	0,05
Fe_2O_3	0,17	0,73	1,24	1,28	1,32	1,33	1,25	1,29	1,69	2,24	0,99	0,59	1,30	0,89	1,20	1,88	1,76	1,62	1,53	1,53	1,7	0,10
FeO	1,11	4,85	8,25	8,54	8,78	8,87	8,31	8,58	11,28	14,94	6,58	3,94	8,65	5,91	8,00	12,52	11,72	10,77	10,18	10,19		
MnO	0,03	0,10	0,14	0,18	0,15	0,15	0,23	0,19	0,19	0,22	0,13	0,02	0,16	0,10	0,15	0,17	0,13	0,36	0,19	0,21	3,7	0,05
MgO	1,90	14,35	11,29	10,64	10,11	7,69	8,40	9,28	9,58	9,84	10,55	1,02	9,31	15,02	7,70	10,16	7,30	10,90	8,91	8,72	3,7	0,01
CaO	8,37	10,56	8,92	7,58	9,56	9,97	10,78	9,14	8,33	9,13	9,49	3,17	8,40	5,08	11,69	10,73	7,44	10,53	10,44	9,15	1,4	0,04
Na_2O	8,33	2,15	2,94	2,48	2,45	1,94	4,30	3,53	3,02	2,31	3,35	6,59	3,77	2,82	4,11	2,55	3,65	2,57	2,98	3,29	3,0	0,01
K_2O	0,13	0,13	0,24	1,63	0,16	1,03	0,30	0,36	0,14	0,33	0,59	0,06	0,46	0,04	0,20	0,24	1,58	0,42	0,66	0,33	3,4	0,01
P_2O_5	0,36	0,02	0,05	0,02	0,11	0,15	0,15	0,14	0,15	0,19	0,09	0,07	0,15	0,31	0,15	0,16	0,56	0,27	0,27	0,21	6,4	0,01
LOI	2,07	3,08	1,82	2,72	3,57	2,55	2,39	3,05	2,68	1,81	1,85	0,49	1,87	3,08	3,55	3,38	1,49	4,11	1,46	1,54		
Total	100,07	100,06	100,05	100,68	100,01	100,08	100,03	99,72	100,47	99,59	100,04	100,07	100,12	99,96	100,92	100,06	100,06	100,05	99,61	100,08		
Mg#	75,4	84,1	70,9	68,9	67,3	60,7	64,3	65,8	60,2	54,0	74,1	31,5	65,7	81,9	63,2	59,1	52,6	64,3	60,9	60,4		
(ppm)																						
Zn	72	28	36	72	96	99	89	99	101	118	58	175	100	74	104	110	100	156	96	94	5,0	2
Cu	3	151	n.d.	3	53	30	73	31	76	37	77	5	50	38	28	97	108	27	92	86	1,9	3
Sc	9	34	39	28	33	31	29	41	37	36	41	9	41	49	30	48	14	17	40	47	3,0	3
Ga	14	10	13	20	15	17	14	15	19	18	14	3	14	9	15	17	23	18	16	14	4,6	3
Ni	2	213	89	102	126	111	44	44	33	86	85	5	28	116	41	141	27	78	119	58	2,6	2
Co	n.d.	30	37	38	37	42	35	57	35	53	21	3	27	43	40	49	25	29	55	52	4,7	2
Cr	3	1069	439	847	324	277	239	336	118	151	752	10	91	106	317	285	66	125	350	96	2,7	2
V	28	172	287	193	288	331	211	242	330	453	255	3	300	158	250	400	129	201	292	300	1,6	2
Rb	5	1	3	9	2	5	3	3	2	1	5	7	7	2	5	4	48	6	10	6	4,7	1
Ba	190	10	16	34	17	20	17	17	21	22	52	112	90	73	48	148	552	116	226	133	3,7	3
Nb	2	1	2	3	2	2	3	2	3	3	6	35	10	12	6	27	68	30	42	24	2,6	1
La	5	2	2	3	2	3	3	3	4	2	4	49	7	11	5	17	55	24	30	16	8,8	2
Ce	10	4	5	10	7	8	9	7	12	7	10	101	16	29	17	37	119	53	58	32	5,2	3
Pb	n.d.	9	7	9	9	6	8	8	9	7	10	-	10	7	8	11	13	11	10	9	-	5
Sr	424	111	103	165	128	59	122	84	190	150	179	99	112	60	146	344	830	454	422	325	1,0	2
Nd	5	2	5	8	8	7	9	7	11	7	7	55	9	18	11	18	46	23	26	16	3,9	2
Zr	36	19	41	86	89	89	109	80	109	79	65	374	79	137	88	150	214	181	189	148	3,2	2
Y	8	7	16	34	31	29	29	27	40	22	15	115	22	31	25	24	37	26	23	21	3,4	1
Hf	n.d.	n.d.	n.d.	2	3	2	2	2	3	2	2	9	2	4	2	4	6	6	5	4	6,6	2
Ta	0,14	0,11	0,10	0,16	0,13	0,14	0,18	0,14	0,24	0,17	0,39	1,71	0,74	0,73	0,39	1,52	5,17	2,09	3,08	1,31	-	0,1
Th	0,20	0,12	0,12	0,19	0,11	0,16	0,19	0,16	0,24	0,21	0,56	3,09	1,04	1,29	0,61	3,01	9,01	2,79	5,15	2,40	-	0,1
U	n.d.	n.d.	n.d.	n.d.	n.d.	n.d.	n.d.	n.d.	0,10	n.d.	0,17	0,69	0,38	0,32	0,18	0,79	2,65	0,97	1,51	0,62	-	0,1

n.d.: not detected; -: not available

Mg# = 100 x molar (MgO/(MgO+FeO))

Fe2O3 = 0,15 FeO

					Data for Wetherill plot3					Ages						
Sample	Identifier	Zrc#	207Pb/206Pb	1s %	207Pb/235U	1s %	206Pb/238U	1s %	Rho	207Pb/206Pb	1s abs	207Pb/235U	1s abs	206Pb/238U	1s abs	% U-Pb disc
MK701	028SMPL	44	0,04953	0,01096	0,17049	0,03704	0,02497	0,00116	0,03	173,0	38,3	159,8	34,7	159,0	7,4	1
MK701	030SMPL	46	0,04822	0,00935	0,16900	0,03220	0,02542	0,00105	0,03	110,1	21,3	158,6	30,2	161,8	6,7	-2
MK701	031SMPL	48	0,05750	0,00739	0,21603	0,02720	0,02725	0,00090	0,03	510,8	65,7	198,6	25,0	173,3	5,7	13
MK701	032SMPL	49	0,06092	0,01290	0,20677	0,04274	0,02462	0,00124	0,03	636,4	134,8	190,8	39,4	156,8	7,9	18
MK701	033SMPL	50	0,05481	0,01077	0,18696	0,03599	0,02474	0,00110	0,03	404,5	79,5	174,0	33,5	157,5	7,0	9
MK701	034SMPL	51	0,07643	0,01994	0,26894	0,06807	0,02552	0,00171	0,03	1106,4	288,7	241,8	61,2	162,4	10,9	33
MK701	035SMPL	52	0,04880	0,01366	0,16903	0,04660	0,02513	0,00134	0,03	138,2	38,7	158,6	43,7	160,0	8,5	-1
MK701	036SMPL	52	0,05752	0,01113	0,19056	0,03608	0,02403	0,00108	0,03	511,5	99,0	177,1	33,5	153,1	6,9	14
MK701	037SMPL	54	0,06645	0,02123	0,23550	0,07332	0,02571	0,00195	0,03	820,6	262,1	214,7	66,9	163,6	12,4	24
MK701	038SMPL	55	0,05282	0,01143	0,17333	0,03673	0,02381	0,00114	0,03	321,1	69,5	162,3	34,4	151,7	7,3	7
MK701	039SMPL	56	0,06198	0,01634	0,20731	0,05354	0,02427	0,00139	0,03	673,4	177,5	191,3	49,4	154,6	8,8	19
MK701	040SMPL	58	0,06477	0,01550	0,23484	0,05489	0,02631	0,00147	0,03	766,9	183,5	214,2	50,1	167,4	9,4	22
MK701	041SMPL	60	0,07393	0,01771	0,27369	0,06382	0,02686	0,00160	0,03	1039,6	249,1	245,6	57,3	170,9	10,2	30
MK701	042SMPL	62	0,06962	0,01362	0,24710	0,04702	0,02575	0,00128	0,03	917,2	179,4	224,2	42,7	163,9	8,1	27
MK701	043SMPL	67	0,04877	0,00914	0,16973	0,03126	0,02525	0,00100	0,03	136,8	25,6	159,2	29,3	160,8	6,4	-1
MK701	044SMPL	67	0,05051	0,00906	0,16069	0,02832	0,02308	0,00088	0,03	218,5	39,2	151,3	26,7	147,1	5,6	3
MK701	045SMPL	65	0,06680	0,01493	0,22919	0,04992	0,02490	0,00135	0,03	831,5	185,9	209,5	45,6	158,5	8,6	24
MK701	046SMPL	64	0,05920	0,01499	0,19097	0,04730	0,02341	0,00133	0,03	574,5	145,4	177,5	43,9	149,2	8,5	16
MK701	047SMPL	63	0,06084	0,01648	0,21746	0,05767	0,02593	0,00153	0,03	633,6	171,6	199,8	53,0	165,0	9,7	17
MK704	006SMPL	102	0,14613	0,05964	0,46959	0,18446	0,02331	0,00265	0,01	2301,1	939,1	390,9	153,5	148,5	16,9	62,0
MK704	007SMPL	103	0,11194	0,04617	0,30321	0,11826	0,01965	0,00268	0,02	1831,1	755,3	268,9	104,9	125,4	17,1	53,4
MK704	008SMPL	104	0,04726	0,00654	0,13712	0,01865	0,02104	0,00058	0,03	62,4	8,6	130,5	17,7	134,2	3,7	-2,9
MK704	009SMPL	99	0,05430	0,00659	0,16383	0,01945	0,02188	0,00059	0,03	383,5	46,6	154,1	18,3	139,5	3,8	9,4
MK704	011SMPL	101	0,09112	0,06908	0,27171	0,20260	0,02163	0,00303	0,01	1449,1	1098,6	244,1	182,0	137,9	19,3	43,5
MK704	012SMPL	97	0,06109	0,04544	0,18603	0,13643	0,02209	0,00282	0,02	642,4	477,8	173,2	127,0	140,9	18,0	18,7
MK704	013SMPL	98	0,20596	0,07381	0,78283	0,26600	0,02756	0,00324	0,01	2874,0	1029,9	587,1	199,5	175,3	20,6	70,1
MK704	014SMPL	94	0,10205	0,02269	0,32878	0,07072	0,02336	0,00135	0,02	1661,7	369,4	288,6	62,1	148,9	8,6	48,4
MK704	015SMPL	95	0,04824	0,01563	0,13810	0,04416	0,02076	0,00110	0,03	111,1	36,0	131,4	42,0	132,5	7,0	-0,8
MK704	016SMPL	92	0,04898	0,00992	0,15475	0,03073	0,02292	0,00094	0,03	146,9	29,7	146,1	29,0	146,1	6,0	0,0
MK704	017SMPL	92	0,05379	0,01307	0,16093	0,03833	0,02169	0,00108	0,03	362,3	88,0	151,5	36,1	138,3	6,9	8,7
MK704	020SMPL	89	0,17214	0,05794	0,63282	0,20108	0,02667	0,00304	0,02	2578,6	867,9	497,9	158,2	169,7	19,4	65,9
MK704	022SMPL	91	0,20529	0,07192	0,71746	0,23523	0,02535	0,00322	0,01	2868,7	1005,0	549,2	180,1	161,4	20,5	70,6
MK704	023SMPL	86	0,05211	0,01502	0,15181	0,04299	0,02114	0,00118	0,03	290,2	83,7	143,5	40,6	134,9	7,6	6,0
MK704	024SMPL	86	0,04837	0,00944	0,13589	0,02599	0,02037	0,00080	0,03	117,4	22,9	129,4	24,7	130,0	5,1	-0,5
MK704	025SMPL	87	0,04940	0,00686	0,14663	0,01989	0,02153	0,00066	0,03	166,9	23,2	138,9	18,9	137,3	4,2	1,2
MK704	026SMPL	88	0,04873	0,01217	0,14273	0,03497	0,02125	0,00105	0,03	134,9	33,7	135,5	33,2	135,6	6,7	-0,1
MK705A	006SMPL	68	0,08052	0,01687	0,20194	0,04105	0,01819	0,00100	0,02	1209,8	253,4	186,8	38,0	116,2	6,4	38
MK705A	007SMPL	68	0,04839	0,01394	0,12208	0,03461	0,01829	0,00101	0,03	118,4	34,1	117,0	33,2	116,8	6,4	0
MK705A	008SMPL	69	0,04940	0,01793	0,11177	0,03998	0,01641	0,00108	0,03	166,9	60,6	107,6	38,5	104,9	6,9	2
MK705A	009SMPL	70	0,04886	0,02105	0,11243	0,04772	0,01669	0,00130	0,03	141,1	60,8	108,2	45,9	106,7	8,3	1
MK705A	011SMPL	72	0,04728	0,00881	0,11880	0,02176	0,01822	0,00072	0,03	63,4	11,8	114,0	20,9	116,4	4,6	-2
MK705A	013SMPL	76	0,04746	0,02533	0,12160	0,06409	0,01858	0,00161	0,03	72,4	38,7	116,5	61,4	118,7	10,3	-2
MK705A	014SMPL	77	0,07011	0,02586	0,17882	0,06450	0,01850	0,00150	0,02	931,6	343,7	167,0	60,3	118,2	9,6	29
MK705A	015SMPL	78	0,04842	0,01066	0,11976	0,02586	0,01795	0,00084	0,03	119,8	26,4	114,9	24,8	114,7	5,4	0
MK705A	016SMPL	78	0,05236	0,00982	0,12803	0,02361	0,01774	0,00071	0,03	301,2	56,5	122,3	22,6	113,4	4,5	7
MK705A	017SMPL	79	0,11763	0,03004	0,32032	0,07807	0,01975	0,00159	0,02	1920,5	490,5	282,1	68,8	126,1	10,2	55
MK705A	018SMPL	80	0,06425	0,01631	0,16674	0,04139	0,01882	0,00108	0,03	749,9	190,3	156,6	38,9	120,2	6,9	23
MK705A	021SMPL	83	0,04824	0,01122	0,10811	0,02476	0,01626	0,00072	0,03	111,1	25,8	104,2	23,9	104,0	4,6	0
MK705A	022SMPL	85	0,07358	0,01738	0,17739	0,04076	0,01749	0,00104	0,03	1030,0	243,3	165,8	38,1	111,8	6,6	33

Composition				Isotopic Ratios							
Th/ U a	Pb* (pg) b	Pbc (pg) c	Pb*/ Pbc d	206Pb/ 204Pb e	207Pb/ 206Pb f	±2σ %	207Pb/ 235U f	±2σ %	206Pb/ 238U f	±2σ %	Corr. coef.
2.14	7.97	0.50	16	687	0.04671	1.6	0.04198	1.7	0.0065216	0.14	0.724

Dates (Ma)								
207Pb/ 206Pb g	±2σ abs	207Pb/ 235U g	±2σ abs	206Pb/ 238U g	±2σ abs	206Pb/ 238U <Th> h	±2σ abs	% disc i
33	38	41.76	0.68	41.904	0.059	41.946	0.070	-25.79

a Th contents calculated from radiogenic 208Pb and 230Th-corrected 206Pb/238U date of the sample, assuming concordance between U-Pb Th-Pb systems.
b Total mass of radiogenic Pb.
c Total mass of common Pb.
d Ratio of radiogenic Pb (including 208Pb) to common Pb.
e Measured ratio corrected for fractionation and spike contribution only.
f Measured ratios corrected for fractionation, tracer and blank.
g Isotopic dates calculated using λ238 = 1,55125E-10 (Jaffey et al. 1971) and λ235 = 9,8485E-10 (Jaffey et al. 1971).
h Corrected for initial Th/U disequilibrium using radiogenic 208Pb and Th/U[magma] = 3.50000.
i % discordance = 100 - (100 * (206Pb/238U date) / (207Pb/206Pb date))